Inducible and reversible inhibition of miRNA-mediated gene repression *in vivo.*

Gaspare La Rocca[1]*, Bryan King[1]*, Bing Shui[2], Xiaoyi Li[1,3], Minsi Zhang[1], Kemal Akat[4], Paul Ogrodowski[1], Chiara Mastroleo[1], Kevin Chen[1], Vincenzo Cavalieri[5], Yilun Ma[6], Viviana Anelli[7], Doron Betel[8], Joana A. Vidigal[9], Thomas Tuschl[4], Gunter Meister[10], Craig B. Thompson[1], Tullia Lindsten[11], Kevin M. Haigis[2] and Andrea Ventura[1]

[1]Cancer Biology & Genetics Program, Memorial Sloan Kettering Cancer Center, New York, NY, USA. [2]Department of Cancer Biology, Dana-Farber Cancer Institute, Boston, MA, USA.

[3]Louis V. Gerstner Jr. Graduate School of Biomedical Sciences, Memorial Sloan Kettering Cancer Center, New York, NY 10065, USA.

[4]Laboratory of RNA Molecular Biology, The Rockefeller University, New York, NY, USA.

[5]Department of Biological, Chemical and Pharmaceutical Sciences and Technologies, University of Palermo, Palermo, Italy.

[6]Weill Cornell/Rockefeller/Sloan-Kettering Tri-Institutional MD-PhD Program, New York, NY, USA.

[7]Center of Integrative Biology, University of Trento, Trento, Italy.

[8]Hem/Oncology, Medicine and Institute for Computational Biomedicine, Weill Cornell Medicine, New York, NY, USA.

[9]Laboratory of Biochemistry and Molecular Biology, National Cancer Institute, Bethesda, MD, USA. [10]Regensburg Center for Biochemistry, University of Regensburg, Germany.

[11]Immunology Program, Memorial Sloan Kettering Cancer Center, New York, NY, USA.

*These authors contributed equally.

email: laroccag@mskcc.org; venturaa@mskcc.org

Abstract

Although virtually all gene networks are predicted to be controlled by miRNAs, the contribution of this important layer of gene regulation to tissue homeostasis in adult animals remains unclear. Gain and loss of function experiments have provided key insights into the specific function of individual miRNAs, but effective genetic tools to study the functional consequences of global inhibition of miRNA activity *in vivo* are lacking. Here we report the generation and characterization of a genetically engineered mouse strain in which miRNA-mediated gene repression can be reversibly inhibited without affecting miRNA biogenesis or abundance. We demonstrate the usefulness of this strategy by investigating the consequences of acute inhibition of miRNA function in adult animals. We find that different tissues and organs respond differently to global loss of miRNA function. While miRNA-mediated gene repression is essential for the homeostasis of the heart and the skeletal muscle, it is largely dispensable in the majority of other organs. Even in tissues where it is not required for homeostasis, such as the intestine and hematopoietic system, miRNA activity can become essential during regeneration following acute injury. These data support a model where many metazoan tissues primarily rely on miRNA function to respond to potentially pathogenic events.

Introduction

MicroRNAs (miRNAs) are short non-coding RNAs that in Metazoa repress gene expression at the post-transcriptional level by binding to partially complementary sequences on target mRNAs (Bartel, 2009, 2018; Eichhorn et al., 2014; Izaurralde, 2015).

MiRNAs act as part of a large ribonucleoprotein complex known as the miRNA-Induced Silencing Complex (miRISC). In mammals, the Argonaute protein family (AGO1-4) and the Trinucleotide Repeat-Containing gene 6 protein family (TNRC6A/GW182, TNRC6B and TNRC6C) are the core components of the miRISC. AGO binds to the miRNA, and facilitates its interaction with target mRNAs (Schirle et al., 2014). In turn, TNRC6 binds to AGO and recruits the decapping and deadenlyation complexes, leading to degradation of target mRNAs (Braun et al., 2011; Chekulaeva et al., 2011; Chen et al., 2009; Chen et al., 2014; Fabian et al., 2011; Guo et al., 2010a; Huntzinger et al., 2013; Lazzaretti et al., 2009; Nishihara et al., 2013; Rehwinkel et al., 2005; Till et al., 2007).

Although miRNAs are abundantly expressed in embryonic and adult mouse tissues, and computational and experimental analyses indicate that they target components of virtually every cellular process (Flynt and Lai, 2008), animals harboring targeted deletion of single miRNA genes are often indistinguishable from their wild type counterparts (Abdellatif, 2012; Chivukula et al., 2014; Cimmino et al., 2005; Liu et al., 2008; Park et al., 2010; van Rooij et al., 2007; Vechetti et al., 2019; Williams et al., 2009). One explanation for these observations is that the redundant functions of related miRNAs may buffer the emergence of obvious phenotypes in mutant animals (Bartel, 2009, 2018). Interestingly, however, clear phenotypes often emerge in mutant adult animals when exposed to external or internal perturbations (Chivukula et al., 2014; Mendell and Olson, 2012; van Rooij et al., 2007). These observations suggest that, at least in some contexts, miRNA function is conditionally, rather than constitutively, required to carry on cellular processes.

Previous efforts to investigate the consequences of global inhibition of miRNA function have relied upon the targeted deletion of the core miRNA biogenesis factors DICER, DROSHA, and

DGCR8 (Treiber et al., 2019). Several animal models harboring conditional or constitutive knockout alleles of these genes have been generated (Bernstein et al., 2003; Chong et al., 2008; Hebert et al., 2010; Huang et al., 2012; JnBaptiste et al., 2017; Kanellopoulou et al., 2005; Kobayashi et al., 2015; Kumar et al., 2007; Wang et al., 2007). Although these strategies have provided important insights into miRNA biology, they suffer from several limitations.

First, inactivation of these gene products is known to have other consequences in addition to impairing miRNA biogenesis. For instance, DICER is involved in epigenetic regulation in the nucleus in a miRNA-independent manner (Fukagawa et al., 2004; Giles et al., 2010; Gullerova and Proudfoot, 2012; Okamura and Lai, 2008; Song and Rossi, 2017; Tam et al., 2008), and is essential to metabolize transcripts from short interspersed nuclear elements, predominantly Alu RNAs in humans and B1 and B2 RNAs in rodents (Kaneko et al., 2011). DROSHA, on the other hand, regulates the expression of several coding and non-coding RNAs by directly cleaving stem–loop structures embedded within the transcripts (Chong et al., 2010). Furthermore, DICER and DROSHA are also involved in the DNA-damage response (Francia et al., 2012) (Michelini et al., 2017), and DGCR8 regulates the maturation of small nucleolar RNAs and of some long non-coding RNAs (Cirera-Salinas et al., 2017; Macias et al., 2015). Consequently, the phenotypes observed in these models cannot be solely attributed to inhibition of miRNA activity.

Another limitation of conditional ablation of miRNA-biogenesis genes *in vivo* is that due to their high stability mature miRNAs can persist for several days after their biogenesis is inhibited. For example, four weeks after near complete conditional ablation of *Dicer1* in the muscle, the levels of the highest expressed miRNAs were found to be only reduced by 30-40% and their expression remained substantial even 18 months later (Vechetti et al., 2019). This complicates

the interpretation of experiments based on temporally controlled conditional ablation of these biogenesis factors, especially in non-proliferating tissues.

Third, a subset of mammalian miRNAs does not rely on the canonical biosynthesis pathway, and therefore their expression and activity are not affected by inactivation of the core miRNA biogenesis factors (Cheloufi et al., 2010; Chong et al., 2010; Cifuentes et al., 2010; Kim et al., 2016; Okamura et al., 2007; Ruby et al., 2007; Yang and Lai, 2011).

Finally, these genetic approaches are not reversible and therefore these animal models cannot be used to study the effects of transient inhibition of miRNA function.

To circumvent these limitations, we have generated a novel genetically engineered mouse strain that allows inducible and reversible disassembly of the miRISC, thereby achieving controllable inhibition of miRNA-mediated gene repression *in vivo* without affecting small RNA biogenesis. To address the reliance of adult tissues on miRNA-mediated gene repression, we have used this novel strain to investigate the consequences of acute inhibition of the miRISC under homeostatic conditions, and during tissue regeneration.

Results

Inhibition of the miRNA pathway through peptide-mediated disruption of the miRISC.

Multiple motifs within the N-terminal domain of TNRC6 proteins contain regularly spaced tryptophan residues which mediate the interaction between AGO and TNRC6 by inserting into conserved hydrophobic pockets located on AGO's Piwi domain (Lian et al., 2009; Sheu-Gruttadauria and MacRae, 2018).

A peptide encompassing one of the AGO-interacting motifs of human TNRC6B has been previously employed as an alternative to antibody-based approaches to efficiently pull down all AGO family members from cell and tissue extracts (Hauptmann et al., 2015; Pfaff et al., 2013). This peptide, named T6B, competes with endogenous TNRC6 proteins for binding to AGOs. However, as it lacks the domains necessary for the recruitment of de-capping and de-adenylation factors, it prevents the assembly of the full miRISC, thus resulting in effective inhibition of miRISC-mediated gene repression in cells (Danner et al., 2017; Hauptmann et al., 2015).

Based on these results, we reasoned that temporally and spatially controlled expression of a T6B transgene in animals would offer the unprecedented opportunity to study the consequences of acute and reversible inhibition of miRNA function *in vivo* without interfering with miRNA biogenesis or abundance (**Figure 1A**).

To test the suitability of this approach, we first investigated the dynamics of interaction between T6B and the miRISC in mouse and human cell lines. We employed a previously reported size exclusion chromatography (SEC)-based assay (La Rocca et al., 2015; Olejniczak et al., 2013) to analyze the molecular weight of AGO-containing complexes in lysates from cells expressing either a doxycycline-inducible FLAG-HA-T6B-YFP fusion protein (hereafter referred to as T6B), or a mutant version (hereafter referred to as $T6B^{Mut}$) incapable of binding to AGO (**Figure 1-figure supplement 1**). We reasoned that if T6B expression prevents AGO from stably binding to TNRC6 and its targets, AGO proteins should be detected in fractions corresponding to approximately 120-130 kDa, the sum of the molecular weights of AGO (approximately 95 kDa) and the T6B fusion protein (approximately 30 kDa). In contrast, unperturbed AGO complexes that are part of the fully assembled miRISC bound to mRNAs

should elute in the void of the column, which contains complexes larger than 2 MDa (**Figure 1B**).

As expected, in lysates from cells expressing no T6B or T6B^{Mut} AGO2 and TNRC6A were mostly detected in the high molecular weight fractions, indicating the presence of target-bound miRISC (**Figure 1C**). In contrast, AGO2 and TNRC6A were nearly completely depleted from the high molecular weight fractions in lysates from cells expressing T6B (**Figure 1C**). Moreover, while AGO2, TNRC6A and the polyA-binding protein 1 (PABP1) co-fractionated in lysates from control cells, they eluted in different fractions in lysates from T6B-expressing cells (**Figure 1C**), indicating that T6B leads to loss of interactions between the miRISC components and mRNAs. As expected based on the strong evolutionary conservation of human and mouse AGO and TNRC6 proteins (Pfaff et al., 2013; Zielezinski and Karlowski, 2015; Zipprich et al., 2009), we obtained identical results when human T6B was expressed in mouse embryo fibroblasts (MEFs) (**Figure 1-figure supplement 2**).

To test whether the redistribution of AGO-containing complexes induced by T6B expression was mirrored by a loss of miRNA-mediated gene repression, we performed RNAseq analysis on MEFs expressing T6B or T6B^{Mut}. Cells expressing T6B displayed marked and selective de-repression of predicted mRNA targets for expressed miRNAs (**Figure 1D**). The extent of de-repression was roughly proportional to the abundance of individual miRNA families, with predicted targets of poorly expressed miRNAs collectively showing modest de-repression compared to targets of more abundantly expressed miRNA families (**Figure 1D**). Importantly, de-repression of miRNA targets was not accompanied by a global change in mature miRNAs levels (**Figure 1E**), consistent with the role of T6B in perturbing the effector step of the miRNA pathway, without affecting miRNA processing.

Of the four mammalian AGO proteins, AGO2 is the only one that has endo-ribonucleolytic activity, which does not require TNRC6 (Liu et al., 2019) and is triggered when the AGO2-loaded small RNA and the target are perfectly complementary (Doench et al., 2003; Liu et al., 2004; Zeng et al., 2003). AGO2's catalytic activity is essential for gene regulation in the germline. For example, in mouse oocytes, AGO2 loaded with endogenous small-interfering RNAs (endo-siRNAs) mediates the cleavage of coding and non-coding transcripts bearing perfectly complementary sequences (Stein et al., 2015; Tam et al., 2008). In metazoan somatic tissues, in contrast, AGO2 catalytic activity is mainly involved in the biogenesis of miR-486 and miR-451 in the hematopoietic system (Cheloufi et al., 2010; Jee et al., 2018), and in occasional instances of miRNA-directed cleavage of mRNAs (Yekta et al., 2004).

Importantly, T6B expression does not interfere with the ability of synthetic siRNAs to cleave perfectly complementary endogenous targets (**Figure 1F**), indicating that AGO2's catalytic function is not affected by the binding of T6B, and implying that the loading of small RNAs onto AGOs is also not perturbed by T6B.

Collectively these results demonstrate that ectopic T6B expression in mammalian cells causes global inhibition of miRISC function with minimal perturbation of the expression of mature miRNAs, and with preservation of AGO2's endo-nucleolytic activity.

Generation of a mouse strain with inducible expression of a T6B transgene.

To apply this general strategy to an *in vivo* setting, we next generated mouse embryonic stem cells (mESCs) expressing a doxycycline-inducible T6B transgene. We used a knock-in approach in which the doxycycline-inducible transgene is inserted into the *Col1a1* locus of

mESC expressing the reverse tetracycline-controlled transactivator (rtTA) under the control of the endogenous *Rosa26* promoter (Beard et al., 2006) (**Figure 2A**). Targeted mESCs were tested for the ability to express the T6B transgene in response to doxycycline (**Figure 2-figure supplement 1**) and then used to generate mice with genotype $Rosa26^{rtTA/rtTA}$; $Col1a1^{T6B/T6B}$ (hereafter $R26^{T6B}$). $Rosa26^{rtTA/rtTA}$; $Col1a1^{+/+}$ mice, with untargeted *Col1a1* loci but expressing rtTA served as negative controls (hereafter $R26^{CTL}$).

Upon doxycycline administration we observed strong expression of T6B in $R26^{T6B}$ mice and across most adult tissues (**Figure 2B**). Notable exceptions were the central nervous system (**Figure 2B, Figure 2-figure supplement 2**), probably due to low blood-brain barrier penetration of doxycycline, and the skeletal muscle and the heart, most likely due to low expression of the rtTA transgene in these tissues (Premsrirut et al., 2011).

When doxycycline was administered in the diet, T6B became detectable after 24h, reached a plateau after three days, and completely disappeared four days after doxycycline removal from the diet (**Figure 2C**).

Because colon and liver expressed uniformly high levels of T6B in response to doxycycline, we used these tissues to test the effects of T6B expression on miRISC activity *in vivo*. Co-IP experiments using antibodies directed to T6B confirmed the interaction between AGO and T6B in these tissues (**Figure 2D, Figure 2-figure supplement 3**). Expression of T6B resulted in nearly complete disassembly of the miRISC, as indicated by the elution shift of AGO from the high molecular weight to low molecular weight fractions in both tissues (**Figure 2E, Figure 2-figure supplement 4**). Importantly, doxycycline removal from the diet led to a complete reconstitution of the miRISC, as indicated by the reappearance of AGO2 in the high molecular weight fractions (**Figure 2E**).

To test whether T6B expression also resulted in inhibition of miRNA-mediated gene repression *in vivo*, we performed RNAseq on total RNAs extracted from the liver and colon of $R26^{T6B}$ and $R26^{CTL}$ mice kept on doxycycline-containing diet for one week. As shown in **Figure 2F**, T6B expression resulted in marked de-repression of miRNA targets in both tissues.

Based on these results we conclude that T6B expression allows acute and reversible disruption of the miRISC, and concomitant inhibition of miRNA function *in vivo*.

Consequences of miRISC disruption in adult tissues under homeostatic conditions.

Given the central role of miRNAs in gene regulatory networks, one might expect widespread phenotypes emerging when miRISC function is systemically inhibited. Consistent with this hypothesis, inhibition of miRISC starting either at conception (**Figure 3A**) or at mid-gestation caused developmental defects and perinatal lethality in $R26^{T6B}$ mice (**Figure 3B, Figure 3-figure supplement 1**). Histological examination of hematoxylin-eosin-stained sections of P0 $R26^{T6B}$ pups treated with Doxycycline starting at mid-gestation confirmed a general delay in development and reduced growth, but no specific organ defects. Surprisingly, however, adult $R26^{T6B}$ mice kept on doxycycline diet for up to two months remained healthy and appeared normal upon macroscopic and histopathologic examination.

Detailed examination of the intestine confirmed extensive T6B expression in the epithelium and in the mesenchymal compartment (**Figure 3-figure supplement 2**), but no architectural abnormalities were observed (**Figure 3C**). Cells in the crypts showed no significant changes in expression pattern of Ki67 protein (**Figure 3-figure supplement 3**), suggesting that the proliferation and turnover of the epithelium is maintained even in absence of a functional

miRISC. No significant change in the number of goblet cells was detected throughout the intestine (**Figure 3-figure supplement 4**), and mice maintained normal body mass throughout the period of doxycycline treatment (**Figure 3-figure supplement 5**), suggesting that general intestinal functions were not affected.

Although no obvious macroscopic, functional, or architectural abnormalities were caused by T6B expression in the intestine, we observed a reduction in lysozyme expression in Paneth cells in the crypts (**Figure 3D**, upper row). However, this phenotype was reversible, as lysozyme signal in the crypts returned to normal levels when doxycycline was removed from the diet (**Figure 3D**, lower row), suggesting that T6B expression did not affect neither the viability of intestinal stem cells, nor their self-renewal ability.

Complete blood counts showed a modest, but significant, decrease in erythrocytes volume (MCV) and hemoglobin content (MCH) in $R26^{T6B}$ RBCs (**Figure 3E, Figure 3-figure supplement 6**), analogously to what reported in mice harboring targeted deletion of miR-451 (Patrick et al., 2010). Flow cytometric analysis of bone marrow showed a 3-fold depletion in Pre-B cells as well as a significant decrease in immature and mature circulating B cells in $R26^{T6B}$ mice. We also observed a reciprocal increase in the frequency of Pro-B cells in the bone marrow of these animals (**Figure 3F, Figure 3-figure supplement 7**). These results are reminiscent of the partial block in B cell differentiation observed upon deletion of the miR-17~92 cluster (Ventura et al., 2008).

Further characterization of hematopoietic stem cells showed that the number of long-term repopulating hematopoietic stem cells (LT-HSC) was unaffected after 3 weeks of doxycycline exposure. However, we observed a modest decrease in short-term repopulating HSCs (ST-

HSCs) and a concomitant increase in multipotent progenitors (MPPs) relative to controls (**Figure 3G, Figure 3-figure supplement 8**).

Collectively, these data suggest that in a subset of adult tissues miRISC function can be suppressed with minimal or no consequences on the ability of these tissues to maintain homeostasis.

miRISC disruption impairs the regeneration of injured colon epithelium.

Several studies have shown that the phenotype caused by targeted deletion of individual miRNAs often manifests only after the mutant animals are subjected to “stress” (Chivukula et al., 2014; Leung and Sharp, 2010; Mendell and Olson, 2012; van Rooij et al., 2007). For example, ablation of miR-143/145 causes no apparent phenotype under homeostasis but severely impairs the ability of the mutant animals to respond to acute damage to the intestinal epithelium (Chivukula et al., 2014).

Prompted by these reports, and by our initial observation that prolonged T6B expression does not substantially affect intestinal homeostasis, we tested the consequences of miRISC disruption on the regenerating intestine. A cohort of $R26^{T6B}$ and $R26^{CTL}$ mice were kept on doxycycline-containing diet for ten days, after which they were treated with dextran sulfate sodium (DSS), which induces severe colitis in mice (Chivukula et al., 2014; Okayasu et al., 1990).

A significant and progressive loss of body mass was observed in both groups during DSS treatment and two days following DSS removal (**Figure 4A**). However, $R26^{T6B}$ mice lost body mass more rapidly than controls and reached critical health conditions seven days after DSS

removal. Three days after DSS removal, control animals started to regain weight, reaching the initial body mass within five days after DSS removal (**Figure 4A**). In contrast, $R26^{T6B}$ mice failed to fully recover (**Figure 4A**), and all reached a humane endpoint within five days after DSS removal from the diet (**Figure 4B**).

Histological analysis confirmed that DSS treatment induced the disruption of the architecture of the epithelium, and the appearance of ulcerative areas to a similar extent in both $R26^{T6B}$ and $R26^{CTL}$ control mice (**Figure 4C, Figure 4-figure supplement 1**). In contrast, although five days after DSS removal the integrity of the colonic epithelium of control mice was largely reestablished with the exception of isolated dysplastic areas (**Figure 4-figure supplement 2**), extensive ulcerated regions persisted in the colon of $R26^{T6B}$ mice (**Figure 4C**). Importantly, we observed the presence of dysplastic epithelium in $R26^{T6B}$ mice during and after DSS treatment, indicating that miRISC disruption does not completely abolish the potential of cells to proliferate, as also confirmed by Ki67 staining (**Figure 4D**). Therefore, we speculate that other factors, such as impaired stem cell maintenance or differentiation, may be responsible for the increased susceptibility of T6B-expressing colon to DSS treatment.

Chivukula and colleagues have shown that defective intestinal regeneration in the colon of miR-143/145-deficient mice is associated with upregulation of the miRNA-143 target IGFBP5 in the mesenchymal compartment. The increased levels of IGFBP5 protein cause the inhibition of IGF1R signaling in the epithelium through a non-cell autonomous mechanism, which ultimately prevented epithelial regeneration (Chivukula et al., 2014). Consistent with their findings, in situ hybridization analyses in the colon of DSS-treated $R26^{T6B}$ mice showed a significant upregulation of IGFBP5 mRNA in the mesenchymal compartment compared to controls (**Figure 4E**). The extent of de-repression of IGFBP5 was comparable to that

296 previously observed in miRNA-143/145 knockout mice (Chivukula et al., 2014), providing
297 further evidence that T6B-mediated miRISC disassembly is an effective strategy to globally
298 inhibit miRNA function *in vivo*.

299 Collectively, these results support a model whereby miRNA-mediated gene regulation, while
300 dispensable to maintain normal colon homeostasis, becomes critical for its regeneration
301 following acute damage.

302

303 **miRISC disruption impairs regeneration of the hematopoietic system.**

304 To further characterize the consequences of miRISC inhibition during tissue regeneration, we
305 explored the possibility that other tissues may adopt a similar dynamic reliance on miRNA
306 function.

307 Along with the intestinal epithelium, blood is one of the most rapidly turned over tissues in
308 mice. Hematopoietic stem cells (HSCs) reside as a predominantly quiescent population in the
309 bone marrow and are rapidly induced to re-enter the cell cycle in response to external cues,
310 such as infection or injury (Ng and Alexander, 2017). Furthermore, HSCs can be readily
311 isolated by flow cytometry and transplanted, allowing the study of mechanisms underlying
312 regeneration at the single cell level.

313 To test the consequences of miRISC disruption in the regenerating hematopoietic system, we
314 treated $R26^{T6B}$ and $R26^{CTL}$ mice on doxycycline-containing diet with a single dose of the
315 cytotoxic drug 5-fluorouracil (5FU). 5-FU selectively depletes rapidly proliferating
316 hematopoietic progenitors and leads to a compensatory increase in LT-HSC proliferation. Flow
317 cytometry analysis of the bone marrow seven days after 5FU-injection showed that T6B

318 expression prevented this compensatory increase in LT-HSC. We observed an identical
319 phenotype when $R26^{T6B}$ and $R26^{CTL}$ mice that were bled repeatedly over a 3-week period to
320 induce LT-HSC to re-enter the cell cycle (**Figure 5A**).

321 The decreased number of HSCs in the bone marrow of $R26^{T6B}$ mice after a single 5-FU
322 challenge compared to controls, suggested that miRISC disruption impaired HSCs' ability to
323 re-enter the cell cycle and regenerate the hematopoietic compartment. Consistent with this
324 hypothesis, when injected with repetitive 5-FU doses, $R26^{T6B}$ mice showed significantly shorter
325 survival compared to controls (**Figure 5B**).

326 To measure the regenerative capacity of HSCs more directly in a context where T6B would
327 only be expressed in hematopoietic cells, we performed competitive transplantation of T6B-
328 expressing ($CD45.2^+$) and wild-type ($CD45.1^+$) bone marrows (1:1 ratio) into lethally irradiated
329 hosts. The recipient animals were divided into four groups as shown in Figure 5C: (i) a control
330 group that was never administered doxycycline; (ii) a group maintained on a doxycycline-
331 containing diet throughout the duration of the experiment (8 weeks); (iii) a group treated with
332 doxycycline starting 4 weeks after transplant; and (iv) a group that was on doxycycline for only
333 the first 4 weeks after transplant. Blood samples were taken at 4 and 8 weeks following the
334 start of the experiment for analysis (**Figure 5C**). This experiment was designed to test the
335 prediction that expression of T6B during the first 4 weeks following transplant, when the
336 regenerative demand is highest and when we hypothesize miRNA-mediated gene repression
337 is required, would more severely affect the ability of donor cells to contribute to the recipient
338 hematopoietic reconstitution compared to T6B expression after homeostasis is reestablished.

339 Consistent with this prediction, mice that were administered doxycycline in the first 4 weeks
340 post-transplant had significantly fewer $CD45.2^+$ peripheral blood mononuclear cells (PBMCs)

(Figure 5D). Contribution to the B cell population was particularly impaired by T6B expression but this was reversed once the recipients were taken off of doxycycline, consistent with the developmental block described earlier (**Figure 3D, Figure 3-figure supplement 7**). Interestingly, the decrease in total CD45.2^{+} PBMCs and CD45.2^{+} myeloid cells was not reversed by doxycycline withdrawal, which suggested the T6B-expressing CD45.2^{+} HSCs might have been outcompeted by wild-type CD45.1^{+} HSCs in these recipients (**Figure 5D**). Consistent with this hypothesis we observed a significant reduction in CD45.2^{+} HSCs only in the bone marrow of recipient animals that were fed a doxycycline-containing diet in the first 4 weeks post-transplant (**Figure 5E**).

Taken together, these results support a model where the miRNA-mediated gene regulation is conditionally essential for the maintenance of hematopoietic stem cells during acute regeneration but is largely dispensable under homeostasis.

An essential role for miRNA-mediated gene repression in the skeletal muscle and in the heart.

As previously discussed, we observed low or no expression of T6B in the heart and skeletal muscle of R26^{T6B} mice treated with doxycycline (**Figure 2-figure supplement 2**), consistent with previous reports indicating that rtTA expression from the endogenous *Rosa26* promoter is tissue restricted (Premsrirut et al., 2011). To extend the analysis of the phenotype caused by the loss of miRISC activity to these tissues, we crossed T6B transgenic mice with the *Rosa26-CAGs-rtTA3* strain (Dow et al., 2014) in which the modified chicken beta-actin with CMV-IE enhancer (CAG) promoter (Niwa et al., 1991) drives a more ubiquitous expression of the rtTA variant rtTA3 (hereafter CAG^{T6B}). As expected, the pattern and intensity of T6B expression

upon dox administration in CAG^{T6B} mice and $R26^{T6B}$ mice were largely overlapping, except for the heart and the skeletal muscle, for which significant T6B expression was only observed in CAG^{T6B} mice (**Figure 6A, Figure 2-figure supplement 2**). RNAseq analyses confirmed inhibition of miRNA function in both heart and skeletal muscle of CAG^{T6B} mice upon dox administration (**Figure 6B**).

In contrast to $R26^{T6B}$ mice, CAG^{T6B} mice fed a doxycycline-containing diet showed a progressive decline in body mass (**Figure 6-figure supplement 1**) and died or reached a humane endpoint within 4-6 weeks (**Figure 6C**). The decrease in body mass was not caused by intestinal malabsorption as, similarly to what observed in $R26^{T6B}$ mice, we found no evidence of architectural defects throughout the intestine. In contrast, histopathologic examination of heart and skeletal muscle showed severe alterations in both organs, including dilated cardiomyopathy and diffuse muscular degeneration (**Figure 6D**). All mice also showed necro-inflammatory changes in the liver, variable alterations in the pancreas, and increased urea nitrogen and alanine aminotransferase levels in the serum. Such alterations are likely secondary to congestive heart failure, and/or to severe muscle catabolism as they were not observed in $R26^{T6B}$ mice. Another phenotype that distinguished the $R26^{T6B}$ strain from the CAG^{T6B} strain was the presence in the latter of vasculitis of pulmonary veins (**Figure 6-figure supplement 2)**. A likely explanation is that these lesions are caused by increased pressure in the pulmonary veins secondary to congestive heart failure, but we cannot exclude that they reflect a direct effect of T6B expression on the pulmonary vasculature. Discriminating between these two possibility will require the use of transgenic mice harboring tissue restricted rtTA transgenes.

386 The emergence of severe cardiac and skeletal muscle phenotypes, as opposed to the lack of
387 obvious structural and functional abnormalities in most T6B-expressing tissues, points toward
388 the existence of significant differences among adult tissues in their reliance on the miRNA
389 pathway during homeostasis.

390 ## Discussion

391 We report the generation of a novel genetically engineered mouse strain in which miRISC
392 assembly and function can be temporally and spatially controlled in a reversible manner by a
393 doxycycline-inducible transgene encoding a T6B-YFP fusion protein to address the role(s)
394 miRNA-mediated gene regulation plays *in vivo* in adult tissues.

395 Surprisingly, in most adult tissues, we do not find an essential role for miRNA-mediated gene
396 repression in organ homeostasis. A notable exception are the heart and the skeletal muscle,
397 where miRISC inactivation in adult mice results in acute tissue degeneration and death even in
398 the absence of tissue damage or exogenous stress.

399 Even though miRISC function is not overtly required for the homeostasis of other tissues, we
400 have investigated the consequences of miRNA inhibition in the intestine and in the
401 hematopoietic system of adult mice under homeostatic conditions and during tissue
402 regeneration. These are tissues that periodically respond to external/internal stresses. In both
403 tissues we have found that miRISC activity is dispensable for homeostasis. However, miRNA
404 function becomes essential during tissue regeneration following acute injury. These results
405 lend experimental support to the hypothesis that a major role for miRNA-mediated gene
406 repression is to support tissue adaptation to stress.

In previous studies where *Dicer1* was conditionally ablated in the skeletal muscle of adult mice, muscle regeneration was impaired after acute injury, but no effect on muscle morphology or function was observed during homeostasis (Oikawa et al.; Oikawa et al.; Vechetti et al.). An explanation for this difference is that in the *Dicer1* conditional knockout experiments miRNA levels were only partially reduced even weeks after *Dicer1* ablation, likely reflecting the high stability of these short non-coding RNAs. The T6B mouse strain we describe here overcomes this major limitation and allows the rapid and effective inhibition of miRNA-activity independently from the half-life of these molecules.

In this manuscript we have focused on the role of miRNA-mediated gene repression in adult mice. The same strategy for the acute inhibition of miRISC-activity can in principle be applied to other organisms. We have found that expression of T6B in embryos of both sea urchin (*Paracentrotus lividus*) and zebrafish (*Danio rerio*), induces developmental defects and gene expression changes consistent with the essential role of the miRNA pathway during development (Ambros and Horvitz, 1984; Chalfie et al., 1981; Lee et al., 1993; Reinhart et al., 2000; Song et al., 2012; Wienholds et al., 2003; Wightman et al., 1993) (**Figure 6-figure supplement 3**). Considering that *in vitro* T6B efficiently binds to AGO proteins from different non-mammalian organisms (Hauptmann et al., 2015), these findings are not unexpected, yet they highlight the usefulness of the T6B system for dissecting the miRNA pathway in a variety of animal models.

Despite its many advantages, the T6B mouse strain has also some unique limitations that need to be considered when designing and interpreting experiments.

First, although our biochemical and computational analysis of cells and tissues expressing T6B indicate that the peptide can effectively impair miRISC function, we cannot exclude some

residual miRISC activity even in cells expressing high levels of the T6B transgene. The observation that we can recapitulate phenotypes observed in mice harboring complete targeted deletion of miR-143/145 miRNAs in the intestine (Chivukula et al., 2014) and of miR-17~92 and miR-451 in the hematopoietic system (Koralov et al., 2008; Patrick et al., 2010; Ventura et al., 2008) is reassuring in this respect. For example, consistent with observations made in the regenerating intestine of miRNA-143/145 knockout mice (Chivukula et al., 2014), we did not record any abnormalities or toxicity during the normal intestinal homeostasis of $R26^{T6B}$ mice, whereas T6B expression became lethal during intestinal regeneration. Moreover, in the hematopoietic system, abnormalities were mostly restricted to B cell maturation, which are consistent with a developmental block at the Pro-B to Pre-B transition found in mir17~92 knockout mice (Ventura et al., 2008). Finally, we also observed a statistically significant decrease in hematocrit, erythrocyte volume and hemoglobin content in adult T6B-expressing mice, analogous to what reported in mice harboring targeted deletion of miR-451 (Patrick et al., 2010).

In contrast, some of our results markedly differ from results obtained by conditional ablation of *Dicer1* in mice. For example, conditional knockout of *Dicer1* in the hematopoietic system has been reported to result in the rapid depletion of HSCs (Guo et al., 2010b). Furthermore, the lack of an overt phenotype in the intestine contrasts with previous reports showing that post-natal, conditional deletion of *Dicer1* results in depletion of goblet cells (Biton et al., 2011; McKenna et al., 2010), in addition to abnormal vacuolation and villous distortion in the small intestine (Huang et al., 2012; McKenna et al., 2010). We cannot exclude that these differences are due to an incomplete inactivation of the miRNA pathway in T6B mice, but an alternative explanation is that they reflect the well-characterized miRNA-independent functions of DICER.

Another limitation to be considered is the possibility that T6B expression impairs the activity of other complexes in addition to the miRISC. Although RNAseq analysis of cells expressing T6B has not revealed changes that are not explained by loss of miRNA-mediated gene repression and the phenotypes observed are consistent with loss of miRNA activity, this possibility cannot be formally excluded at this time. Further studies to experimentally identify T6B interactors in cells and tissues will be important to formally address this possibility.

In conclusion, we have developed a novel mouse strain that enables investigating the role of miRNA-mediated gene repression in adult organisms. The body of data presented here suggests that in adult animals miRNAs primarily provide for the ability to adaptively change gene expression in response to the physiologic and pathologic stresses that accompany metazoans' life. It is likely that the specific miRNAs and stresses differ based on the adult organ or tissue being studied and the model we have generated will be useful address these important aspects of miRNA biology.

Acknowledgements

This work was funded by the Starr Foundation's Tri-Institutional Stem Cell Initiative (A.V., T.L., D.B. and T.T.), and by the NIH/NCI (grants R01CA149707 and R01CA245507 to A.V. and P30 CA008748 to C.B.T.). Y.M. was supported by a Medical Scientist Training Program grant from the National Institute of General Medical Sciences of the National Institutes of Health under award number: T32GM007739 to the Weill Cornell/Rockefeller/Sloan Kettering Tri-Institutional MD-PhD Program. We acknowledge the use of the following core facilities at the Memorial Sloan Kettering Cancer Center (MSKCC): The Molecular Cytology Core; The Mouse Genetics

Core Facility; The Laboratory of Comparative Pathology, and the Integrated Genomics Operation Core, funded by the NCI Cancer Center Support Grant (CCSG, P30 CA08748), Cycle for Survival, and the Marie-Josée and Henry R. Kravis Center for Molecular Oncology. We thank Sebastien Monette and Ileana Miranda for their contribution in the phenotypic analysis of $R26^{T6B}$ and CAG^{T6B} mouse strains; Davide Pradella, Rui Gao, Saurabh Yadav and members of the Benezra laboratory for discussion and suggestions. Finally, we thank Jaqueline Candelier for the handling and processing of tissue samples used in the phenotypic analyses of the $R26^{T6B}$ and CAG^{T6B} mouse strains.

Competing interests

Craig B Thompson: C.B.T. is a founder of Agios Pharmaceuticals and a member of its scientific advisory board. He is also a former member of the Board of Directors and stockholder of Merck and Charles River Laboratories. He is a named inventor on patents related to cellular metabolism. Potentially relevant patents on which C.B.T is a named inventor include the following: (i) L-2-hydroxyglutarate and stress induced metabolism (United States Patent #10,450,596). (ii) Single diastereomers of 4-fluoroglutamine and methods of their preparation and use (United States Patent #8,747,809). A complete list of patents can be found at the following link: https://tinyurl.com/y35qvajq. The other authors declare no competing interests.

Data Availability

Datasets generated during this study are deposited at the Gene Expression Omnibus (GEO):

GSE179588 (https://www.ncbi.nlm.nih.gov/geo/query/acc.cgi?acc=GSE179588).

Figure Legends

Figure 1. T6B fusion protein prevents miRISC assembly and impairs miRNA activity *in vitro*. (**A**) Schematics of T6B action: T6B competes with TNRC6 for binding to AGO proteins preventing miRISC assembly. (**B**) Schematics of the size exclusion chromatography (SEC) assay for the fractionation of AGO-containing complexes according to their molecular weight. (**C**) SEC profiling of miRISC components upon T6B expression: Total lysates from HCT116 cells expressing no fusion protein (upper panel), T6B (middle panel) or $T6B^{Mut}$ (lower panel) were fractionated as described in (B) and immunoblotted to detect AGO2, TNRC6A, T6B and PABP1. For each blot the relative signal intensity was assessed by densitometric analysis. (**D**) RNAseq analysis of total and small RNAs isolated from MEFs cell lines expressing either no fusion protein, T6B or $T6B^{Mut}$ (n = 3 for each cell line). Upper panel: bubble plot of target de-repression against miRNA abundance. The mean log2Fold Change (T6B or $T6B^{Mut}$ vs control) of predicted targets for each conserved miRNA family was calculated, converted to a z-score and is plotted on the x-axis against the miRNA family abundance (log of the sum of read counts for each member of the family). The size of each circle is proportional to the number of predicted targets. A positive z score indicates that the targets for that family are preferentially upregulated upon T6B expression, while a negative score would indicate preferential downregulation. Expression of T6B, but not of $T6B^{Mut}$, causes preferential upregulation of miRNA targets of the most miRNA families and the effect is roughly proportional to each miRNA family abundance. Lower panel: cumulative distribution plot of predicted let-7 targets compared to background in T6B-expressing MEFs. (**E**) Scatter plots of miRNA abundance as determined by small-RNAseq of total RNA extracted from MEFs expressing either T6B or $T6B^{Mut}$ (n = 3 for each cell line). Each dot represents a miRNA in miRbase. (**F**) Effect of T6B

expression on AGO2 slicing activity. MEFs expressing either T6B or T6B^{Mut} were transfected with siRNAs targeting GAPDH mRNA (siGAPDH) or with scramble siRNA (siCTL). Levels of GAPDH, T6B and tubulin were assessed by immunoblot 72 hours post-transfection. T6B and T6B^{Mut} have slightly different migration on PAGE, as previously observed by Hauptmann at al. (Hauptmann et al., 2015).

The following figure supplements and source data are available for Figure 1:

Figure 1- figure supplement 1. Binding of T6B with AGO protein *in vitro*.

Figure 1- figure supplement 2. T6B-mediated disassembly of the miRISC in murine cells.

Figure 1- source data 1. RNAseq, differential gene expression MEFs.

Figure 1 - source data 2. zScores and miRNA family abundance, MEFs.

Figure 1 - source data 3. small RNAseq, microRNA counts, MEFs.

Figure 1 - source data 4. Unedited blots shown in Figure 1C.

Figure 1 - source data 5. Uncropped blots shown in Figure 1C.

Figure 1 - source data 6. Unedited blots shown in Figure 1F.

Figure 1 - source data 7. Uncropped blots shown in Figure 1F.

Figure 1 - figure supplement 1 - source data 1. Unedited blots shown in Figure 1 - figure supplement 1.

Figure 1 - figure supplement 1 - source data 2. Uncropped blots shown in Figure 1 - figure supplement 1.

Figure 1 - figure supplement 2 - source data 1. Unedited blots shown in Figure 1 - figure supplement 2.

Figure 1 - figure supplement 2 - source data 2. Uncropped blots shown in Figure 1 - figure supplement 2.

Figure 2. Expression of T6B reversibly blocks miRISC assembly and inhibits miRNA function *in vivo*. (**A**) Schematic of the targeting strategy to generate the T6B mouse. The construct contains a flippase recognition target site (frt) that allows homing into the *Col1a1* locus when electroporated together with a vector expressing the Flippase recombinase into KH2 (*Col1a1-frt/Rosa26-rtTA*) murine embryonic stem cells. KH2 also express the rtTA trans-activator driven by the endogenous *Rosa26* (R26) promoter. (**B**) Immunofluorescence imaging performed using an anti-YFP antibody, showing T6B expression in a panel of tissues of adult $R26^{T6B}$ mice fed doxycycline for 7 days. Tissues from $R26^{CTL}$ (carrying the rtTA allele but not the T6B allele) were used as negative controls. (**C**) Protein lysates from the liver of $R26^{T6B}$ mice on or off doxycycline-containing chow for the indicated number of days were resolved by SDS-PAGE and Western blotting was performed with anti-HA antibody to detect expression of the T6B transgene. (**D**) Co-IP experiments using an anti-YFP antibody showing interaction between AGO and T6B in total liver extracts from T6B mice on doxycycline containing chow. (**E**) SEC elution profile of AGO2-containing complexes in liver lysates from T6B mice euthanized at the indicated time points after doxycycline administration. Notice the shift of AGO2 from the high molecular weight fractions to the low molecular weight fractions after 5 days of doxycycline treatment and the reconstitution of the full miRISC after removal of doxycycline from the diet. (**F-G**) Total RNA extracted from the large intestine (F) and the liver (G) of $R26^{CTL}$ and $R26^{T6B}$ mice was subjected to RNAseq (n = 3 for each strain). Left panel: scatter plot showing the

564 effect of T6B expression on targets of all miRNA families were generated as described in
565 Figure 1D. The abundance of each miRNA family was calculated using dataset from Isakova et
566 al. (Isakova et al.). Right panel: Representative cumulative distribution plot of log2 fold
567 changes in expression of predicted targets of the indicated miRNA families.

568 The following figure supplements and source data are available for Figure 2:

569 Figure 2 - figure supplement 1. Epifluorescence imaging showing T6B expression in selected
570 ESC clones.

571 Figure 2 - figure supplement 2. IF imaging showing T6B expression in selected adult tissues.

572 Figure 2 - figure supplement 3. Co-IP of T6B and AGO2 in colon extracts.

573 Figure 2 - figure supplement 4. Size exclusion chromatography on extracts of T6B-expressing
574 liver and colon.

575 Figure 2 - source data 1. RNAseq, differential gene expression, colon and liver.

576 Figure 2 - source data 2. Z-Scores and miRNA families abundance, colon and liver.

577 Figure 2 - source data 3. Unedited blots shown in Figure 2C.

578 Figure 2 - source data 4. Uncropped blots shown in Figure 2C.

579 Figure 2 - source data 5. Unedited blots shown in Figure 2D.

580 Figure 2 - source data 6. Uncropped blots shown in Figure 2D.

581 Figure 2 - source data 7. Unedited blots shown in Figure 2E.

582 Figure 2 - source data 8. Uncropped blots shown in Figure 2E.

Figure 2 - figure supplement 1 - source data 1. Unedited blots shown in Figure 2 - figure supplement 1.

Figure 2 - figure supplement 1 - source data 2. Uncropped blots shown in Figure 2 - figure supplement 1.

Figure 2 - figure supplement 3 - source data 1. Unedited blots shown in Figure 2 - figure supplement 3.

Figure 2 - figure supplement 3 - source data 2. Uncropped blots shown in Figure 2 - figure supplement 3.

Figure 2- figure supplement 4 - source data 1. Unedited blots shown in Figure 2 - figure supplement 4.

Figure 2- figure supplement 4 - source data 2. Uncropped blots shown in Figure 2 - figure supplement 4.

595

596 **Figure 3**. Phenotypic analysis of R26^{T6B} mice during homeostasis. (**A**) *Rosa26*$^{+/+}$*; Col1a1*$^{T6B/T6B}$
597 females were crossed with *Rosa26rtTA/+; Col1a1*$^{T6B/T6B}$ males and doxycycline was
598 administered by chow starting at 0.5 d.p.c. No viable pups positive for both the rtTA and T6B
599 allele were observed (n = 15, p-value = 0.002, Fisher exact test). (**B**) Pregnant females were
600 kept on doxycycline diet from E13.5 to E18.5 and the pups delivered on E18.5 by c-section.
601 Note the significantly smaller size of *Rosa26*$^{rtTA/rtTA}$*; Col1a1*$^{T6B/T6B}$ embryos relative to
602 *Rosa26*$^{rtTA/rtTA}$ *;Col1a1*$^{+/+}$ control littermates. Lower row: YFP detection by epifluorescence in
603 E18.5 pups of the indicated genotypes. (**C**) Comparison of intestine architecture in H&E
604 sections from R26^{T6B} and R26^{CTL} mice (n = 3 for each genotype) maintained on doxycycline for
605 2 months. (**D**) Immunofluorescence imaging of the small intestine of R26^{T6B} and R26^{CTL} mice
606 (n = 3-5 for each genotype) kept on doxycycline diet for a month (upper row), showing a
607 reduction in lysozyme expression in Paneth cells in the crypts. Lysozyme expression in R26^{T6B}
608 mice returned to normal levels upon removal of doxycycline from the diet (lower row). (**E**)
609 Peripheral blood analysis conducted in R26^{T6B} and R26^{CTL} mice (R26^{CTL} n = 4; R26^{T6B} n = 5).
610 (**F)** Flow cytometric analysis of bone marrow of R26^{T6B} and R26^{CTL} mice kept on doxycycline
611 diet for 3 weeks showing developmental block at the Pro-B to Pre-B. p values (from left to
612 right): *p = 0.0348, **p = 0.0023, *p = 0.0340, **p = 0.0004, unpaired t-test. R26^{CTL} n = 4;
613 R26^{T6B} n = 5. (**G**) Flow cytometry analysis of the bone marrow of control and R26^{T6B} mice kept
614 on doxycycline diet for 3 weeks. p values (from left to right): p = 0.0994, **p = 0.0092, **p =
615 0.0085, *p = 0.0312, unpaired t-test. R26^{CTL} n = 4; R26^{T6B} n = 5.

616 The following figure supplements are available for figure 3:

617 Figure 3 - figure supplement 1. Body weight and morphology of T6B-expressing embryos.

Figure 3 - figure supplement 2. IF imaging showing T6B expression in small and large intestine of $R26^{T6B}$ mice.

Figure 3 - figure supplement 3. Ki67 expression in colon and small intestine of $R26^{T6B}$ and $R26^{CTL}$ mice.

Figure 3 - figure supplement 4. Detection of goblet cells in $R26^{T6B}$ and $R26^{CTL}$.

Figure 3 - figure supplement 5. Comparison of body weight of $R26^{T6B}$ and $R26^{CTL}$ mice.

Figure 3 - figure supplement 6 - Summary of complete blood count in $R26^{T6B}$ and $R26^{CTL}$ mice.

Figure 3 - figure supplement 7. Flow cytometry plots related to Figure 3f.

Figure 3 - figure supplement 8. Flow cytometry plots related to Figure 3g.

Figure 4. T6B-induced block of miRISC assembly leads to impaired intestinal regeneration. (**A**) $R26^{T6B}$ and $R26^{CTL}$ mice (n = 6 for each genotype) kept on doxycycline diet were treated with Dextran Sodium Sulphate (DSS) for 5 days to induce inflammatory colitis and their weight was monitored daily. Data are presented as mean ± s.d. p values (from left to right): *p = 0.034, *p = 0.005, *p = 0.029, *p = 0.024, *p = 0.011, from unpaired t test. (**B**) Kaplan-Meier curves of animals treated with DSS as described in panel (A). p value from log-rank test (**C**) Representative hematoxylin-eosin-stained sections of intestine of $R26^{T6B}$ and $R26^{CTL}$ mice (n = 3 for each genotype) at different time points pre- and post-DSS treatment. (**D**) Ki67 immunostaining of section of intestine at the indicated time points. (**E**) Sections from the large intestine of control and T6B mice euthanized at day 13 were subjected to RNA *in situ* hybridization with a probe against the IGFBP5 transcript. The results show increased levels of

639 IGFBP5 mRNA in ulcerated areas of $R26^{T6B}$ as compared to controls (n = 4 for each
640 genotype).

641 The following figure supplements are available for Figure 4:

642 Figure 4 - figure supplement 1. Extent of DSS-induced injury in the colon of $R26^{T6B}$ and $R26^{CTL}$
643 mice.

644 Figure 4 - figure supplement 2. Evidence of residual dysplasia in colon of $R26^{CTL}$ mice post-
645 DSS treatment.

646

Figure 5. T6B-induced block of miRISC assembly impairs the regeneration of the hematopoietic system. (**A**) Long term HSC in the bone marrow of $R26^{T6B}$ and $R26^{CTL}$ mice treated with 5-FU or subjected to repeated bleeding (n = 5 for each genotype). Mice were maintained on doxycycline containing diet throughout the experiment. (**B**) Kaplan-Meier plots of $R26^{T6B}$ (n = 5) and $R26^{CTL}$ (n = 5) mice treated weekly with 5-FU for seven weeks. (**C**) Schematic of the bone marrow transplantation experiments: T6B was induced at different time points post-transplantation, and multilineage reconstitution was assessed at the indicated time points by FACS. (**D**) FACS analysis conducted on the peripheral blood of irradiated recipients transplanted 1:1 with T6B-expressing and wild-type bone marrow, and maintained on doxycycline diet according to scheme shown in panel C. Data are presented as mean ± s.d. *p < 0.05, **p < 0.01, ***p < 0.001, one-way ANOVA. off > off, n = 9; off > on, n = 10; on > off, n = 8; on >on, n = 8. (**E**) FACS analysis showing the frequency of T6B-extressing HSCs in the bone marrow of transplanted recipient mice kept on doxycycline diet according to scheme shown in panel c. off > off, n = 5; off > on, n = 5; on > off, n = 4; on > on, n = 5, one-way ANOVA.

Figure 6. The miRNA pathway is essential in heart and skeletal muscle during homeostasis. (**A**) Detection of T6B expression with an anti-YFP antibody in the heart and skeletal muscle of $R26^{T6B}$, CAG^{T6B}, and $R26^{CTL}$ mice maintained on doxycycline containing diet for 7 days. (**B**) Total RNA extracted from the heart (upper panel) and the skeletal muscle (lower panel) of CAG^{CTL} and CAG^{T6B} mice (n = 3 for each strain) maintained on dox for 7 days was analyzed by RNAseq. Left panels: Scatter plot showing the effect of T6B expression on targets of conserved miRNA families were generated as described in figure 1D. The abundance of each miRNA family was calculated using dataset from Isakova et al. (Isakova et al.). Right panels: Representative cumulative distribution plot of log2 fold changes in expression of predicted targets of the indicated miRNA families. (**C**) Kaplan-Meier curves of CAG^{T6B} and CAG^{CTL} mice (n = 8 for each genotype) maintained on doxycycline throughout the duration of the experiment. p value from log-rank test. (**D**) Upper row: representative H&E staining showing marked dilation of the four cardiac chambers in hearts of CAG^{T6B} mice compared to controls (n = 9 for each genotype). Despite having thinner walls, the histomorphology of ventricular cardiomyofibers were within normal limits. Bottom row: representative H&E staining showing degenerative and regenerative changes in the skeletal muscle of the hind limbs of CAG^{T6B} mice compared to controls (n = 9 for each genotype).

The following figure supplements and source data are available for Figure 6:

Figure 6 - figure supplement 1. Comparison of body weight of CAG^{T6B} and CAG^{CTL} mice.

Figure 6 - figure supplement 2. H&E staining showing vasculitis of pulmonary veins in CAG^{T6B} mice.

Figure 6 – figure supplement 3. Effects of T6B expression in *P. lividus* and *Danio rerio*

Figure 6 – source data 1. RNAseq, heart and muscle.

Figure 6 – source data 2. Z-scores and miRNA family abundance, heart and muscle.

Materials and Methods

Key resource table

Reagent type (species) or resource	Designation	Source or reference	Identifiers	Additional information
strain, strain background *(M. musculus)*	T6B	This paper	Stock #036470	The T6Bwt allele is integrated in the *Col1a1* locus
strain, strain background *(M. musculus)*	CD45.1^{+} C57BL/6 (BoyJ)	Jackson lab	RRID:IMSR_JAX:002014	Carries the differential *Ptprc*^{a} pan leukocyte marker
strain, strain background *(M. musculus)*	C57BL/6J	Jackson lab	RRID:IMSR_JAX:000664	
strain, strain background *(M. musculus)*	*Rosa26-CAGs-rtTA3*	Jackson lab	RRID:IMSR_JAX:029627	The CAG promoter drives the expression of rtTA3
cell line *(M. musculus)*	KH2	PMID: 16400644	RRID:CVCL_C317	Embryonic stem cells
cell line *(M. musculus)*	DR4	ATCC	RRID:CVCL_VK72	Irradiated feeder cells
transfected construct *(M. musculus)*	Silencer GAPDH siRNA	Thermo Fisher	#AM4624	
transfected construct *(M. musculus)*	Negative Control 1 siRNA	Thermo Fisher	#AM4611	Nontargeting control
antibody	anti-E-Cadherin (Mouse monoclonal)	BD	#610181	IF: (1:750)
antibody	Anti-Lysozyme (Rabbit polyclonal)	Thermo Fisher	#RB-372-A1	IF: (1:200)
antibody	anti-PH3 (Mouse monoclonal)	Cell Signaling	#970	IF: (1:200)
antibody	anti-YFP (Rabbit polyclonal)	Invitrogen	#A11122	IF: (1:250)
antibody	anti-Ki67 (Rabbit monoclonal)	Cell Signaling	#12202	IF: (1:400)
antibody	anti-Rabbit IgG, Alexa Fluor 488	ThermoFisher	#A11034	IF: (1:250)

	(Goat polyclonal)			
antibody	anti-Mouse IgG2a, Alexa Fluor 594 (Goat polyclonal)	ThermoFisher	# A-21135	IF: (1:250)
antibody	Anti-GFP (Chicken polyclonal)	Abcam	#ab13970	IF : (1:250)
antibody	Rat IgG (Rat Polyclonal)	Sigma	#I-8015	IF: (1:250)
antibody	anti-GW182 (Rabbit polyclonal)	Bethyl	#A302-329A	WB: (1:1000, in 5% milk)
antibody	anti-Ago2 (Rabbit monoclonal)	Cell Signaling	#2897	WB: (1:1000)
antibody	anti-RPL26 (Rabbit polyclonal)	Bethyl	#A300-686A	WB: (1:1000)
antibody	anti-GAPDH (Mouse monoclonal)	Sigma	#G8795	WB: (1:2000)
antibody	anti-βActin (Mouse monoclonal)	Sigma	#A2228	WB: (1:2000)
antibody	anti-Tubulin (Mouse monoclonal)	Sigma-Aldrich	#T9026	WB: (1:2000)
antibody	anti-HA (Rabbit monoclonal)	Cell Signaling	#C29F4	WB: (1:1000)
antibody	anti-Rabbit IgG, HRP-conjugated (Donkey polyclonal)	(GE Healthcare	#NA934	WB: (1:10000)
antibody	anti-Mouse IgG, HRP-conjugated (Sheep polyclonal)	(GE Healthcare	#NA931	WB: (1:10000)
antibody	Anti-AGO2 (Mouse monoclonal)	WAKO	#011-22033	IP: (1 μg/100μL)
antibody	Anti-AGO1-4 (Mouse monoclonal)	EMD Millipore	#MABE56	IP: (1 μg/100μL)
antibody	anti-FLAG (Mouse monoclonal)	Cell Signaling	#8146S	IP: (1 μg/100μL)
antibody	anti-HA (Mouse monoclonal)	Cell Signaling	#2367S	IP: (1 μg/100μL)
antibody	Anti-IgG1 isotype	Cell Signaling	#5415	IP: (1 μg/100μL)

	(Mouse monoclonal)			
recombinant DNA reagent	pCAGGS-flpE-puro (plasmid)	Addgene	RRID:Addgene_20733	Flippase recombinase-expressing vector
recombinant DNA reagent	pgk-ATG-frt plasmid	Addgene	RRID:Addgene_20734	
sequence-based reagent	Col1a1 common _F	This paper	PCR primers	AATCATCCCAGGTGCACAGCATTGCGG
sequenced-based reagent	Col1a1 wildtype _R	This paper	PCR primers	CTTTGAGGGCTCATGAACCTCCCAGG
sequenced-based reagent	Col1a1 mutant _R	This paper	PCR primers	ATCAAGGAAACCCTGGACTACTGCG
sequenced-based reagent	R26_F	This paper	PCR primers	AAAGTCGCTCTGAGTTGTTAT
sequenced-based reagent	R26a_R	This paper	PCR primers	GCGAAGAGTTTGTCCTCAACC
sequenced-based reagent	R26b_R	This paper	PCR primers	CCTCCAATTTTACACCTGTTC
sequenced-based reagent	T6B-YFP_F	This paper	PCR primers	GACTACAAGGACGACGATGACAAG
sequenced-based reagent	T6B-YFP_R	This paper	PCR primers	GTTACTTGTACAGCTCGTCCATG
commercial assay or kit	RNAscope 2.5 HD Detection Reagent, BROWN	ACD	#320771	
commercial assay or kit	RNAScope Igfbp5 Probe	ACD	#425738	
commercial assay or kit	Superose 6 10/300 GL	Cytiva	#GE17-5172-01	Now available as Increase 10/300 GL, Cytia # GE29-0915-96
commercial assay or kit	Novex NuPAGE SDS/PAGE gel system	Thermo Fisher	#NP0321	
commercial assay or kit	EnVision+ HRP	DAKO, Glostrup, Denmark	#K401111–2, RRID:AB_2827819	
commercial assay or kit	GFP-trap	Chromotek	#gtma-10 RRID:AB_28	

			27592	
commercial assay or kit	TruSeq Stranded mRNA LT Kit,	Illumina	#RS-122-2102	
software, algorithm	OMERO	PMID: 22373911	RRID:SCR_002629	
software, algorithm	STAR v2.5.3a	PMID: 23104886		
software, algorithm	DESeq2	PMID: 25516281	RRID:SCR_015687	
software, algorithm	miRbase version 21	https://www.mirbase.org/		
software, algorithm	TargetScan	PMID: 26267216	RRID:SCR_010845	
chemical compound, drug	Doxycyline-containing Rodent diet	Envigo	#TD01306	625mg/Kg doxycycline
chemical compound, drug	Dextran sulfate sodium (DSS)	Cayman Chemical	#23250	
chemical compound, drug	Surgipath Decalcifier I	Leica Biosystems	#3800400	formic acid solution
other	EDTA-free complete protease inhibitors	Sigma-Aldrich	#11836170001	
other	KnockOut DMEM	GIBCO	#10829018	
other	phosphate inhibitors	Roche	#04906837001	
other	TRIzol Reagent	Thermo Fisher	1#5596026	
other	DAPI stain	Sigma Aldrich	#62248	5 µg/ml
other	Mowiol 4–88	Calbiochem	#475904100GM	Mounting media
other	GlutaMax	GIBCO	#35050061	
other	A/G PLUS-Agarose beads	Santa Cruz	#2003	
other	RIPA buffer	Sigma-Aldrich	# R0278	
other	Lipofectamine RNAiMAX	Thermo Fisher	#13778100	Transfection reagent
other	Alexa Fluor 488 tyramide	Life	B40953	

	signal amplification reagent	Technologies		

690

691 ***Animal models*.** The *Rosa26*$^{rtTA/rtTA}$ *; Col1a1*$^{T6B/T6B}$ (R26^{T6B}) mice were generated by site-
692 specific integration of the transgene coding for the FLAG-HA-T6B-YFP fusion protein within the
693 *Col1a1* locus of KH2 embryonic stem cells (*Col1a1*-frt/*Rosa26 rtTA*) (Beard et al., 2006).
694 Briefly, the FLAG-HA-T6B-YFP (FH-T6B-YFP) DNA fragment was subcloned into the targeting
695 vector, as described in "Vectors and molecular cloning". A mixture of 5µg of the targeting
696 vector and 2.5µg of the pCAGGS-flpE-puro (Addgene #20733), Flippase recombinase-
697 expressing vector were electroporated into KH2 cells, using 4D-Nucleofector core unit (Lonza),
698 following manufacturer's "Primary cells P3" protocol. Selection of targeted clones was initiated
699 48h after electroporation, using 150µg hygromycin per mL of culture medium. 10 days later,
700 individual hygromycin-resistant ES cell clones were analyzed by PCR to confirm correct
701 integration of the knock-in allele. Clones carrying the correctly integrated knock-in allele were
702 genotyped using a three-primer PCR, with the following primers: 1) 5'-
703 AATCATCCCAGGTGCACAGCATTGCGG-3'; 2) 5'-CTTTGAGGGCTCATGAACCTCCCAGG-
704 3'; 3) 5'-ATCAAGGAAACCCTGGACTACTGCG-3'. A 287pb-long PCR product indicates
705 successful integration of the transgene into the *Col1a1* locus, while a 238bp-long PCR product
706 indicates a wild type, untargeted locus. Two independent ES clones were injected into
707 C57BL/6J albino blastocysts and backcrossed the resulting chimeras to C57BL/6J mice to
708 achieve germline transmission of the recombinant allele. F1 animals were then intercrossed to
709 generate animals expressing rtTA from the *Rosa26* locus under control of the *Rosa26*
710 endogenous promoter, while expressing the T6B fusion protein from the *Col1a1* locus under
711 control of the tetracycline-responsive element (TRE) and the minimal CMV promoter. Animals

were genotyped as follows: to assess the presence of the transgene in the *Col1a1* locus, PCR was carried out as for the genotyping of KH2 cells. To assess the presence of the rtTA transgene in the *Rosa26* locus, a three-primer PCR was performed, using the following primers: 1) 5'-AAAGTCGCTCTGAGTTGTTAT-3'; 2) 5'-GCGAAGAGTTTGTCCTCAACC-3'; 3) 5'-CCTCCAATTTTACACCTGTTC-3'. A 350pb-long PCR product indicates the presence of the rtTA transgene into the *Rosa26* locus, while a 297bp-long PCR product indicates the presence of a wild type locus. $CAG^{rtTA/rtTA}$; $Col1a1^{T6B/T6B}$ (CAG^{T6B}) mice were generated by backcrossing $R26^{T6B}$ mice with *Rosa26-CAGs-rtTA3* mice (a gift from Scott Lowe, MSKCC). In the *Rosa26-CAGs-rtTA3* mice, the knock-in allele has the CAG promoter driving the expression of the third-generation reverse tetracycline-regulated transactivator gene (rtTA3), all inserted into the *Gt(ROSA)26Sor* locus. *In vivo* doxycycline-dependent expression of the FLAG-HA-T6B-YFP transgene was achieved by feeding mice chow that contained doxycycline at the concentration of 625mg/Kg (Envigo #TD01306). Mice were maintained and euthanized in accordance with a protocol approved by the Memorial Sloan-Kettering Cancer Center Institutional Animal Care and Use Committee. The T6B transgenic strain has been deposited at the Jackson Laboratory (JAX stock #036470)

***Necropsy, staining and histopathology*.** Mice were euthanized with CO2. Following gross examination all organs were fixed in 10% neutral buffered formalin, followed by decalcification of bone in a formic acid solution (Surgipath Decalcifier I, Leica Biosystems). Tissues were then processed in ethanol and xylene and embedded in paraffin in a Leica ASP6025 tissue processor. Paraffin blocks were sectioned at 5 microns, stained with hematoxylin and eosin (H&E), and examined by a board-certified veterinary pathologist. The following tissues were

735 processed and examined: heart, thymus, lungs, liver, gallbladder, kidneys, pancreas, stomach,
736 duodenum, jejunum, ileum, cecum, colon, lymph nodes (submandibular, mesenteric), salivary
737 glands, skin (trunk and head), urinary bladder, uterus, cervix, vagina, ovaries, oviducts,
738 adrenal glands, spleen, thyroid gland, esophagus, trachea, spinal cord, vertebrae, sternum,
739 femur, tibia, stifle join, skeletal muscle, nerves, skull, nasal cavity, oral cavity, teeth, ears, eyes,
740 pituitary gland, brain. To detect goblet cells in the intestine, the AB/PAS kit (ThermoFisher
741 #87023) was used according to the manufacturer's instructions.

742

743 ***Immunofluorescence***. For the staining of intestine sections shown in Figure 3 and Figure 3-
744 figure supplement 2, formalin-fixed, paraffin-embedded (FFPE) slides were deparaffinized and
745 rehydrated according to a standard xylene/ethanol series. After heat-induced epitope retrieval
746 in sodium citrate (pH6), tissue sections were permeabilized in triton X-100, blocked, and
747 incubated with the following 1º antibodies: PH3 (Cell Signaling #970) at 1:200 dilution;
748 Lysozyme (ThermoFisher #RB-372-A1) at 1:200 dilution; E-Cadherin (BD#610181) at 1:750
749 dilution; YFP (Invitrogen #A11122) at 1:250 dilution; Ki67 (Cell Signaling #12202) at 1:400
750 dilution. Next, cells were washed with PBS containing 0.05% Triton X, and incubated with the
751 following 2º antibodies: Goat anti-Rabbit IgG, Alexa Fluor 488 (ThermoFisher #A11034) at
752 1:250 dilution; Goat anti-Mouse IgG2a, Alexa Fluor 594 (ThermoFisher #A11029) at 1:250
753 dilution. For the staining of tissue sections shown in Figure 2, Figure 4 and Figure 2-figure
754 supplement 2, FFPE tissue sections were cut at 5 µm and heated at 58°C for 1 hr. The
755 antibody against GFP (Abcam, ab13970, 2µg/ml) was incubated for 1 hr and detected with
756 Leica Bond RX. Appropriate species-matched secondary antibody and Leica Bond Polymer
757 anti-rabbit HRP were used, followed by Alexa Fluor 488 tyramide signal amplification reagent

(Life Technologies, B40953). After staining, slides were washed in PBS and incubated in 5 µg/ml 4',6-diamidino-2-phenylindole (DAPI) (Sigma Aldrich) in PBS (Sigma Aldrich) for 5 min, rinsed in PBS, and mounted in Mowiol 4–88 (Calbiochem). Slides were kept overnight at -20°C before imaging.

Immunohistochemistry. For IHC, deparaffinized sections were subjected to antigen retrieval and processed with the EnVision+ HRP kit (K401111–2, DAKO, Glostrup, Denmark) according to the manufacturer's instructions. A primary polyclonal antibody against Ki67 (Cell Signaling #12202) at 1:400 dilution was diluted in Antibody Diluent (DAKO #S0809) and incubated overnight at 4°C. Next, sections were incubated in the provided anti-rabbit HRP-labeled polymer reagent and detection was performed according to the manufacturer's protocol. Images were acquired using an Olympus BX-UCB slide scanner.

RNA in situ hybridization. 5µm sections were obtained from formalin-fixed, paraffin-embedded (FFPE) colons from age/sex-matched mice. Before staining, tissue slides were deparaffinized, rehydrated and permeabilized according to standard procedures. Detection was carried out using RNAscope 2.5 HD Detection Reagent, BROWN (ACD # 320771), with a specific RNAScope Igfbp5 Probe (ACD #425738, according to the manufacturer's instructions.

Serum chemistry and hematology. For serum chemistry, blood was collected into tubes containing a serum separator, the tubes were centrifuged, and the serum was obtained for analysis. Serum chemistry was performed on a Beckman Coulter AU680 analyzer and the

concentration of the following analytes was determined: alkaline phosphatase, alanine aminotransferase, aspartate aminotransferase, creatine kinase, gamma-glutamyl transpeptidase, albumin, total protein, globulin, total bilirubin, blood urea nitrogen, creatinine, cholesterol, triglycerides, glucose, calcium, phosphorus, chloride, potassium, and sodium. Na/K ratio, albumin/globulin ratio were calculated. For hematology, blood was collected retro-orbitally into EDTA microtainers. Automated analysis was performed on an IDEXX Procyte DX hematology analyzer.

Dextran sulfate sodium (DSS) treatment and post DSS treatment quantitative analyses. Mice kept in doxycycline-containing chow were treated for 5 days with 4% w/v DSS (FW 40.000) (Cayman Chemical #23250) dissolved in drinking water. Body mass was monitored daily. Measurements of colon length, aggregated length of ulcers, percentage of colon with ulcers, area of ulcers, the number of immune nodules and the area of immune nodules were obtained using OMERO (https://www.openmicroscopy.org/omero/). Measurements of these parameters were used to estimate the extent of damage and colitis induced by DSS treatment. All measurements were acquired from H&E-stained colon sections. Ulcer was defined as regions of colon with complete/partial loss of epithelial structure, accompanied by massive immune infiltrates. Colon length was measured by tracing the length of muscular layer of each colon. Length of ulcer was measured as the added length of each ulcerated region along the colon. Ulcer percentage was calculated as the length of ulcer/length of colon. The area of each individual ulcer was also measured and summed for each animal. Clear immune nodules are visible, showing aggregates of immune cells with high nucleus/cytoplasm ratio. Number and area of the immune nodules were summarized for each animal.

***Tissue isolation and total lysates preparation*.** Organs extracted from 8- to 12-week-old mice, perfused with PBS, were snap-frozen in liquid nitrogen and stored at −80 °C until further processing. To prepare total extract from solid tissues, tissues were pulverized using a mortar, resuspended in 1mL of lysis buffer per cm3 of tissue, and dounce-homogenized with a tight pestle until completely homogenized. Next, extracts were cleared by centrifugation at 20,000 × g for 5 min followed by a second step of centrifugation at 20,000 × g for 5 min. To prepare total extracts from cultured cells, pelleted cells were snap frozen in liquid nitrogen and stored at −80 °C until further processing. Pellets were then resuspended in lysis buffer, incubated for 10 minutes on ice, and cleared by centrifugation at 20,000 × g. Two different lysis buffers were used, depending on the specific downstream application. For IP and size exclusion chromatography, lysates were prepared in SEC buffer (150 mM NaCl, 10 mM Tris-HCl pH 7.5, 2.5 mM MgCl2, 0.01% Triton X-100). For Western blotting applications, lysates were prepared in RIPA buffer (Sigma-Aldrich # R0278). Upon usage, both buffers were supplemented with the addition of EDTA-free complete protease inhibitors (Sigma-Aldrich #11836170001), phosphate inhibitors (Roche #04906837001), and 1mM DTT.

Cell Lines and Culture Conditions. Cell lines were maintained in log-phase growth in a humidified incubator at 37°C, 5% CO2 prior to experimental manipulation. HCT116 colorectal adenocarcinoma cells were obtained from ATCC prior this study and tested negative for Mycoplasma and were maintained in McCoy's medium supplemented with 10% heat-inactivated fetal calf serum (FCS, GIBCO, Cat#16141079), 10 U/ml penicillin/streptomycin, and 2 mM L-glutamine. Mouse embryonic fibroblasts (MEF) were grown in Dulbecco's Modified

826 Eagle Medium (DMEM) supplemented with 10% heat-inactivated fetal calf serum (FCS,
827 GIBCO), 10 U/ml penicillin/streptomycin, and 2 mM L-glutamine. KH2 embryonic stem cells
828 were cultured in gelatin-coated plates in presence of irradiated DR4 Mouse Embryonic
829 Fibroblasts (ThermoFisher #A34966), and maintained in KnockOut DMEM (GIBCO,
830 Cat#10829018), supplemented with 15% FCS (GIBCO), GlutaMax (GIBCO Cat#35050061),
831 100 μM non-essential amino acids (Sigma-Aldrich Cat#M7145), 1000 U/mL leukemia inhibitory
832 factor (LIF, Millipore Cat#ESG1107), 10U/mL penicillin/streptomycin (GIBCO Cat#15070063)
833 and 100 mM 2-Mercaptoethanol (Bio-Rad Cat#1610710), and nucleosides (Millipore Cat#ES-
834 008-D).

835

836 ***Flow cytometry***. Analysis of bone marrow populations was performed by harvesting femurs
837 and tibiae from euthanized mice. Bone marrow was isolated by centrifugation, resuspended in
838 FACS buffer (PBS with 2% fetal calf serum) and passed through a 40μm cell strainer to make
839 a single cell suspension. Nonspecific antibody binding was blocked by incubation with 10μg/ml
840 Rat IgG (Sigma #I-8015) for 15 min on ice. Antibodies used to identify HSCs included a
841 cocktail of biotinylated lineage antibodies (Gr1, CD11b, TER119, B220, CD3, CD4, CD8),
842 CD117 (c-kit) APC (2B8), Sca-1 (D7) PE-cy7, CD150 PE, and CD48 Pacific Blue. B cell
843 progenitors were identified with the following antibodies: B220, CD19, CD25, CD43, IgM, IgD
844 and c-kit. For analysis of peripheral blood mononuclear cells, blood was collected retro-
845 orbitally from live mice into EDTA microtainers. Whole blood was lysed in ACK buffer for 5 min
846 at room temperature, washed with FACS buffer and pelleted prior to antibody staining. Mature
847 blood populations were identified with the following antibodies: CD45.1, CD45.2, Gr1, CD11b,
848 B220, CD3. Cells were incubated with primary antibodies for 45 min, washed once with FACS

buffer and incubated with BV711 streptavidin conjugate for 15 min. All incubations were carried out on ice and protected from light. Antibodies were purchased from Biolegend or eBioscience.

Bone marrow transplantation. 8–12-week-old CD45.1^{+} C57BL/6 (BoyJ) mice (JAX) were lethally irradiated by exposure to 1100cGy of gamma irradiation from a cesium source, administered in two doses, split 4h apart. Bone marrow suspensions from CAG^{T6B} (CD45.2^{+}) and BoyJ mice were counted, mixed 1:1 and transferred intravenously by retro-orbital injection into isofluorane-anesthetized, irradiated recipients.

Size exclusion chromatography (SEC). SEC was performed using a Superose 6 10/300 GL prepacked column (GE Healthcare) equilibrated with SEC buffer essentially as previously described (La Rocca et al., 2015; Olejniczak et al., 2013). Briefly: 400µL (1.5–2 mg) of total extracts precleared by centrifugation were run on the SEC column at a flow rate of 0.3 mL/min. 1mL fractions were collected. Proteins were extracted from each fraction by TCA precipitation following standard procedures, and run on SDS-PAGE gels for Western blotting analysis.

Western blotting and antibodies. Western blotting was performed using the Novex NuPAGE SDS/PAGE gel system (Invitrogen). Total cell lysates were run either on 3–8% Tris-acetate or 4–12% Bis-Tris precast gels, transferred to nitrocellulose membranes, and probed with antibodies specific to proteins of interest. Detection and quantification of blots were performed on Amersham hyperfilm ECL (Cytiva #28906839) and developed on film processor SRX-101A (Konica). Antibodies used for Western blots were obtained from commercial sources as

follows: anti-GW182 (Bethyl #A302-239A), anti-Ago2 (Cell Signaling #2897), anti-PABP1 (Cell Signaling #4992), anti-RPL26 (Bethyl #A300-686A), anti-GAPDH (Sigma #G8795), anti-βActin (Sigma #A2228) anti-GFP (Roche #11814460001), anti-Tubulin (Sigma-Aldrich #T9026) anti-HA (Cell Signaling #C29F4), anti-Rabbit IgG, HRP-conjugated (GE Healthcare #NA934), anti-Mouse IgG, HRP-conjugated (GE Healthcare #NA931).

Immunoprecipitation (IP). For IP of AGO-T6B complexes from human HCT116 cells, 500µg of lysates in 500 µL of SEC buffer were incubated for 3 hours with primary antibodies directed to either AGO proteins (WAKO anti-AGO2 #011-22033, EMD Millipore anti-panAGO #MABE56) or directed to T6B-fusion protein (Cell Signaling anti-FLAG #8146S, Cell Signaling anti-HA #2367S) or mouse IgG1 isotype control (Cell Signaling #5415). Next, lysates were incubated with 20µl of protein A/G PLUS-Agarose beads (Santa Cruz #2003) for 1 hour. For IP of AGO-T6B complexes from mouse tissues, 500µg of lysates in 500 µL of SEC buffer were incubated for 2 hours with GFP-trap magnetic agarose beads (Chromotek #gtma-10) or binding control beads (Chromotek #bmab-20). The immune complexes were run on SDS-PAGE and analyzed by Western blotting.

Vectors and molecular cloning. The targeting vector expressing the FH-T6B-YFP under control of TRE and CMV minimal promoter, was generated from a modified version of the pgk-ATG-frt plasmid (Addgene plasmid #20734), in which the region of pgk-ATG-frt comprised between the EcoRI site and the PciI site was substituted with the rabbit β-globin polyadenylation signal (RBG pA). The FH-T6B-YFP DNA insert was generated by PCR using the plasmid pIRES-Neo-FH-T6B-YFP[58] as a template. PCR was carried out using the following

primers: Forward: 5'-GACTACAAGGACGACGATGACAAG-3', Reverse: GTTACTTGTACAGCTCGTCCATG. Next, the modified pgk-ATG-frt, was cut with NcoI, filled-in to produce blunt ends, dephosphorylated and ligated to the PCR-generated FH-T6B-YFP DNA fragment, according to standard subcloning procedures. Below, a scheme of the cloning strategy:

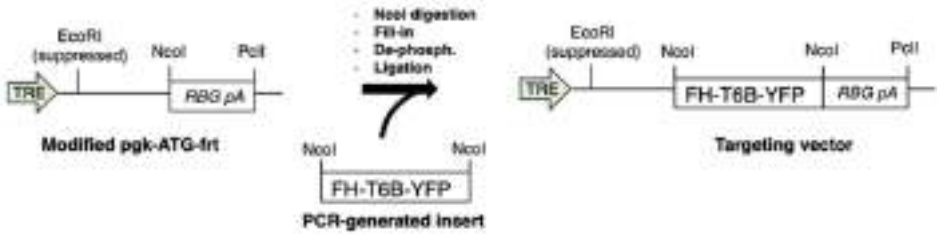

To generated cell lines expressing either FH-T6B-YFP or FH-T6B^{Mut}-YFP fusion proteins in a doxycycline-inducible manner, a modified version of the retroviral vector pSIN-TREtight-HA-UbiC-rtTA3-IRES-Hygro (hereafter TURN vector, a gift from Scott Lowe) was used to transduce commercially available HCT116 and MEFs cell lines. TURN is an all-in-one Tet-on vector that includes: 1) The rtTA3 gene under the human ubiquitin C promoter; 2) The transgene of interest driven by a tetracycline-responsive element (TRE)/CMV promoter. We used the pIRES-Neo-FH-T6B-YFP described in Hauptmann ae al.[58] as a template to generate by PCR the DNA fragments coding either for FH-T6B-YFP or for FH-T6BMut-YFP fusion proteins. DNA fragments were then inserted into the XhoI/EcoRI-digested TURN vector to generate TURN^{T6B} and TURN^{T6Bmut} vectors used for the transduction of parental HCT116 and MEFs.

914 ***Small RNA Transfection.*** Silencer GAPDH siRNA (ThermoFisher AM4624) and Silencer
915 Select Negative Control 1 siRNA (ThermoFisher AM4611). Small RNAs were transfected at 10
916 pM per 1 × 10^6 cells. MEFs were reverse transfected using Lipofectamine RNAiMAX.
917 Lipofectamine RNAiMAX was combined with 20 μM small RNAs at a 4:3 ratio (vol:vol) in Opti-
918 MEM and incubated for 20 min at room temperature. Trypsinized cells were added to culture
919 dishes containing siRNAs and Lipofectamine RNAiMAX at 3.8 × 10^4 cells per centimeter
920 squared. Three volumes of complete medium were added to culture dishes and cells were
921 incubated for 2–3 days before further processing.

922

923 ***Small RNA sequencing****.* Total RNA was extracted from MEFs transduced with the retroviral
924 vectors encoding a doxycycline inducible T6B or $T6B^{mut}$ transgene and cultured in the
925 presence or absence of doxycycline. Small RNA-seq library preparation was as described in
926 (Hafner et al., 2011). Briefly, 1 μg total RNA was ligated to nine distinct pre-adenylated 26-nt
927 3'-adapters with a 5-nt barcode using a mutated and truncated Rnl2 followed by urea gel
928 purification and size selection and 5'-adapter ligation with Rnl1. This ligation reaction was
929 again gel purified and size-selected for fully ligated product and reverse transcribed using
930 SuperScript III RT followed by PCR amplification using Taq polymerase for 25 cycles. The final
931 PCR product was separated on a 2% agarose gel in TBE buffer and extracted using the
932 QIAgen gel extraction kit according to the manufacturer's instructions including all optional
933 steps. After high-throughput sequencing, small RNA reads were aligned to a miRNA genome
934 index built from 1,915 murine pre-miRNA sequences from miRbase version 21(Kozomara et
935 al., 2019)(ftp://mirbase.org/pub/mirbase/21/) using Bowtie v2.4.296. Mature miRNA abundance
936 was calculated by counting reads falling within 4 bps at each of the 5' and 3' end of the

annotated mature miRNAs. miRNA seed family data were downloaded from the TargetScan website at http://www.targetscan.org/mmu_71/mmu_71_data_download/miR_Family_Info.txt.zip. For miRNA family level analysis, read counts mapping to members of the same miRNA family were summed up.

RNAseq analysis. Total RNA from heart, skeletal muscle, colon and liver of sex-matched littermate animals, and total RNA from cell lines was extracted using TRIzol Reagent (Invitrogen) according to manufacturer's instructions and subjected to DNase (QIAGEN) treatment. After RiboGreen quantification and quality control by Agilent BioAnalyzer, 500ng of total RNA with RIN values of 7.0-10 underwent polyA selection and TruSeq library preparation according to instructions provided by Illumina (TruSeq Stranded mRNA LT Kit, catalog # RS-122-2102), with 8 cycles of PCR. Samples were barcoded and run on a HiSeq 4000 in a PE50/50 run, using the HiSeq 3000/4000 SBS Kit (Illumina). An average of 34 million paired reads was generated per sample. The percent of mRNA bases averaged 60% over all samples. Reads were aligned to the standard mouse genome (mm10) using STAR v2.5.3a(Dobin et al., 2013). RNA reads aligned were counted at each gene locus. Expressed genes were subjected to differential gene expression analysis using DESeq2 (Love et al., 2014), log2Fold changes were determined comparing T6B expressing tissues to controls.

Z-score calculation. For each conserved miRNA families the mean log2-fold change of predicted targets, as defined by Targetscan, compared to the rest of the transcriptome (back-ground) was calculated. The means were converted to z-scores as described by Kim and

960 Volsky (Kim and Volsky, 2005): Z-score = (Sm - μ)*$m^{1/2}$*∂^{-1} , where Sm is the mean of log2-
961 fold changes of genes for a given gene set, m is the size of the gene set and μ and ∂ are the
962 mean and the standard deviation of background log2-fold change values.

963

964 ***Real-time quantitative PCR*.** Real-time quantitative PCR analysis to assess the expression
965 levels of the territorial marker genes involved in the developmental gene regulatory network of
966 the sea urchin where conducted as previously described by Cavalieri et al. (Cavalieri et al.,
967 2009). Briefly, total RNA from batches of 150 microinjected embryos was extracted by using
968 the High Pure RNA Isolation kit (Roche). RNA samples were treated with reagents provided by
969 the Turbo DNA-free kit (Ambion) and resuspended in a final volume of 30 μl. Reverse
970 transcription into cDNA was performed in an 80 μl reaction using random hexamers and the
971 TaqMan Reverse Transcription Reagents kit (Applied Biosystems). The resulting cDNA sample
972 was further diluted and the equivalent amount corresponding to one embryo was used as
973 template for Q-PCR analysis. Q-PCR experiments were performed from two different batches
974 and all reactions were run in triplicate on the 7300 Real-Time PCR system (Applied
975 Biosystems) using SYBR Green detection chemistry (Applied Biosystems). ROX was used as
976 a measure of background fluorescence and *MBF-1* and *z12* mRNAs were used as internal
977 controls. At the end of the amplification reactions, a 'melting-curve analysis' was run to confirm
978 the homogeneity of all Q-PCR products. Calculations from Q-PCR raw data were performed by
979 the RQ Study software version 1.2.3 (Applied Biosystems), using the comparative Ct method
980 (Ct). Oligonucleotide primer pairs used for qPCR reactions and amplicon lengths have been
981 described previously (Cavalieri et al., 2008) (Cavalieri et al., 2011) (Cavalieri and Spinelli,
982 2014) (Cavalieri et al., 2017) (Turturici et al., 2018).

References

Abdellatif, M. (2012). Differential expression of microRNAs in different disease states. Circ Res *110*, 638-650.

Ambros, V., and Horvitz, H.R. (1984). Heterochronic mutants of the nematode Caenorhabditis elegans. Science *226*, 409-416.

Bartel, D.P. (2009). MicroRNAs: Target Recognition and Regulatory Functions. Cell *136*, 215-233.

Bartel, D.P. (2018). Metazoan MicroRNAs. Cell *173*, 20-51.

Beard, C., Hochedlinger, K., Plath, K., Wutz, A., and Jaenisch, R. (2006). Efficient method to generate single-copy transgenic mice by site-specific integration in embryonic stem cells. Genesis *44*, 23-28.

Bernstein, E., Kim, S.Y., Carmell, M.A., Murchison, E.P., Alcorn, H., Li, M.Z., Mills, A.A., Elledge, S.J., Anderson, K.V., and Hannon, G.J. (2003). Dicer is essential for mouse development. Nature genetics *35*, 215-217.

Biton, M., Levin, A., Slyper, M., Alkalay, I., Horwitz, E., Mor, H., Kredo-Russo, S., Avnit-Sagi, T., Cojocaru, G., Zreik, F.*, et al.* (2011). Epithelial microRNAs regulate gut mucosal immunity via epithelium-T cell crosstalk. Nature immunology *12*, 239-246.

Braun, J.E., Huntzinger, E., Fauser, M., and Izaurralde, E. (2011). GW182 Proteins Directly Recruit Cytoplasmic Deadenylase Complexes to miRNA Targets. Molecular cell *44*, 120-133.

Cavalieri, V., Di Bernardo, M., Anello, L., and Spinelli, G. (2008). cis-regulatory sequences driving the expression of the Hbox12 homeobox-containing gene in the presumptive aboral ectoderm territory of the Paracentrotus lividus sea urchin embryo. Developmental Biology *321*, 455-469.

Cavalieri, V., Geraci, F., and Spinelli, G. (2017). Diversification of spatiotemporal expression and copy number variation of the echinoid hbox12/pmar1/micro1 multigene family. Plos One *12*.

Cavalieri, V., Guarcello, R., and Spinelli, G. (2011). Specific expression of a TRIM-containing factor in ectoderm cells affects the skeletal morphogenetic program of the sea urchin embryo. Development *138*, 4279-4290.

Cavalieri, V., Melfi, R., and Spinelli, G. (2009). Promoter activity of the sea urchin (Paracentrotus lividus) nucleosomal H3 and H2A and linker H1 alpha-histone genes is modulated by enhancer and chromatin insulator. Nucleic Acids Research *37*, 7407-7415.

Cavalieri, V., and Spinelli, G. (2014). Early asymmetric cues triggering the dorsal/ventral gene regulatory network of the sea urchin embryo. Elife *3*.

1013 Cavalieri, V., and Spinelli, G. (2015a). Ectopic hbox12 Expression Evoked by Histone Deacetylase
1014 Inhibition Disrupts Axial Specification of the Sea Urchin Embryo. PLoS One *10*, e0143860.

1015 Cavalieri, V., and Spinelli, G. (2015b). Symmetry Breaking and Establishment of Dorsal/Ventral Polarity
1016 in the Early Sea Urchin Embryo. Symmetry-Basel *7*, 1721-1733.

1017 Chalfie, M., Horvitz, H.R., and Sulston, J.E. (1981). Mutations That Lead to Reiterations in the Cell
1018 Lineages of C-Elegans. Cell *24*, 59-69.

1019 Chekulaeva, M., Mathys, H., Zipprich, J.T., Attig, J., Colic, M., Parker, R., and Filipowicz, W. (2011).
1020 miRNA repression involves GW182-mediated recruitment of CCR4-NOT through conserved W-
1021 containing motifs. Nature Structural & Molecular Biology *18*, 1218-U1262.

1022 Cheloufi, S., Dos Santos, C.O., Chong, M.M.W., and Hannon, G.J. (2010). A Dicer-independent miRNA
1023 biogenesis pathway that requires Ago catalysis. Nature *465*, 584-U576.

1024 Chen, C.Y.A., Zheng, D.H., Xia, Z.F., and Shyu, A.B. (2009). Ago-TNRC6 triggers microRNA-mediated
1025 decay by promoting two deadenylation steps. Nature Structural & Molecular Biology *16*, 1160-U1166.

1026 Chen, Y., Boland, A., Kuzuoglu-Ozturk, D., Bawankar, P., Loh, B., Chang, C.T., Weichenrieder, O., and
1027 Izaurralde, E. (2014). A DDX6-CNOT1 complex and W-binding pockets in CNOT9 reveal direct links
1028 between miRNA target recognition and silencing. Molecular cell *54*, 737-750.

1029 Chivukula, R.R., Shi, G.L., Acharya, A., Mills, E.W., Zeitels, L.R., Anandam, J.L., Abdelnaby, A.A.,
1030 Balch, G.C., Mansour, J.C., Yopp, A.C.*, et al.* (2014). An Essential Mesenchymal Function for miR-
1031 143/145 in Intestinal Epithelial Regeneration. Cell *157*, 1104-1116.

1032 Chong, M.M., Zhang, G., Cheloufi, S., Neubert, T.A., Hannon, G.J., and Littman, D.R. (2010).
1033 Canonical and alternate functions of the microRNA biogenesis machinery. Genes & development *24*,
1034 1951-1960.

1035 Chong, M.M.W., Rasmussen, J.P., Rudensky, A.Y., and Littman, D.R. (2008). The RNAseIII enzyme
1036 Drosha is critical in T cells for preventing lethal inflammatory disease (vol 205, pg 2005, 2008). Journal
1037 of Experimental Medicine *205*, 2449-2449.

1038 Cifuentes, D., Xue, H., Taylor, D.W., Patnode, H., Mishima, Y., Cheloufi, S., Ma, E., Mane, S., Hannon,
1039 G.J., Lawson, N.D.*, et al.* (2010). A novel miRNA processing pathway independent of Dicer requires
1040 Argonaute2 catalytic activity. Science *328*, 1694-1698.

1041 Cimmino, A., Calin, G.A., Fabbri, M., Iorio, M.V., Ferracin, M., Shimizu, M., Wojcik, S.E., Aqeilan, R.I.,
1042 Zupo, S., Dono, M.*, et al.* (2005). miR-15 and miR-16 induce apoptosis by targeting BCL2. Proceedings
1043 of the National Academy of Sciences of the United States of America *102*, 13944-13949.

1044 Cirera-Salinas, D., Yu, J., Bodak, M., Ngondo, R.P., Herbert, K.M., and Ciaudo, C. (2017).
1045 Noncanonical function of DGCR8 controls mESC exit from pluripotency. J Cell Biol *216*, 355-366.

1046 Danner, J., Pai, B., Wankerl, L., and Meister, G. (2017). Peptide-Based Inhibition of miRNA-Guided
1047 Gene Silencing. Methods Mol Biol *1517*, 199-210.

1048 Dobin, A., Davis, C.A., Schlesinger, F., Drenkow, J., Zaleski, C., Jha, S., Batut, P., Chaisson, M., and
1049 Gingeras, T.R. (2013). STAR: ultrafast universal RNA-seq aligner. Bioinformatics *29*, 15-21.

1050 Doench, J.G., Petersen, C.P., and Sharp, P.A. (2003). siRNAs can function as miRNAs. Genes &
1051 development *17*, 438-442.

1052 Dow, L.E., Nasr, Z., Saborowski, M., Ebbesen, S.H., Manchado, E., Tasdemir, N., Lee, T., Pelletier, J.,
1053 and Lowe, S.W. (2014). Conditional Reverse Tet-Transactivator Mouse Strains for the Efficient
1054 Induction of TRE-Regulated Transgenes in Mice. Plos One *9*.

1055 Eichhorn, S.W., Guo, H.L., McGeary, S.E., Rodriguez-Mias, R.A., Shin, C., Baek, D., Hsu, S.H.,
1056 Ghoshal, K., Villen, J., and Bartel, D.P. (2014). mRNA Destabilization Is the Dominant Effect of
1057 Mammalian MicroRNAs by the Time Substantial Repression Ensues. Molecular cell *56*, 104-115.

1058 Fabian, M.R., Cieplak, M.K., Frank, F., Morita, M., Green, J., Srikumar, T., Nagar, B., Yamamoto, T.,
1059 Raught, B., Duchaine, T.F.*, et al.* (2011). miRNA-mediated deadenylation is orchestrated by GW182
1060 through two conserved motifs that interact with CCR4-NOT. Nature Structural & Molecular Biology *18*,
1061 1211-U1252.

1062 Flynt, A.S., and Lai, E.C. (2008). Biological principles of microRNA-mediated regulation: shared themes
1063 amid diversity. Nat Rev Genet *9*, 831-842.

1064 Francia, S., Michelini, F., Saxena, A., Tang, D., de Hoon, M., Anelli, V., Mione, M., Carninci, P., and
1065 d'Adda di Fagagna, F. (2012). Site-specific DICER and DROSHA RNA products control the DNA-
1066 damage response. Nature *488*, 231-235.

1067 Fukagawa, T., Nogami, M., Yoshikawa, M., Ikeno, M., Okazaki, T., Takami, Y., Nakayama, T., and
1068 Oshimura, M. (2004). Dicer is essential for formation of the heterochromatin structure in vertebrate
1069 cells. Nat Cell Biol *6*, 784-791.

1070 Giles, K.E., Ghirlando, R., and Felsenfeld, G. (2010). Maintenance of a constitutive heterochromatin
1071 domain in vertebrates by a Dicer-dependent mechanism. Nat Cell Biol *12*, 94-99; sup pp 91-96.

1072 Gullerova, M., and Proudfoot, N.J. (2012). Convergent transcription induces transcriptional gene
1073 silencing in fission yeast and mammalian cells. Nat Struct Mol Biol *19*, 1193-1201.

1074 Guo, H., Ingolia, N.T., Weissman, J.S., and Bartel, D.P. (2010a). Mammalian microRNAs
1075 predominantly act to decrease target mRNA levels. Nature *466*, 835-840.

1076 Guo, S., Lu, J., Schlanger, R., Zhang, H., Wang, J.Y., Fox, M.C., Purton, L.E., Fleming, H.H., Cobb, B.,
1077 Merkenschlager, M.*, et al.* (2010b). MicroRNA miR-125a controls hematopoietic stem cell number.
1078 Proceedings of the National Academy of Sciences of the United States of America *107*, 14229-14234.

Hafner, M., Renwick, N., Brown, M., Mihailovic, A., Holoch, D., Lin, C., Pena, J.T.G., Nusbaum, J.D., Morozov, P., Ludwig, J.*, et al.* (2011). RNA-ligase-dependent biases in miRNA representation in deep-sequenced small RNA cDNA libraries. Rna *17*, 1697-1712.

Hauptmann, J., Schraivogel, D., Bruckmann, A., Manickavel, S., Jakob, L., Eichner, N., Pfaff, J., Urban, M., Sprunck, S., Hafner, M.*, et al.* (2015). Biochemical isolation of Argonaute protein complexes by Ago-APP. Proceedings of the National Academy of Sciences of the United States of America *112*, 11841-11845.

Hebert, S.S., Papadopoulou, A.S., Smith, P., Galas, M.C., Planel, E., Silahtaroglu, A.N., Sergeant, N., Buee, L., and De Strooper, B. (2010). Genetic ablation of Dicer in adult forebrain neurons results in abnormal tau hyperphosphorylation and neurodegeneration. Hum Mol Genet *19*, 3959-3969.

Huang, T.C., Sahasrabuddhe, N.A., Kim, M.S., Getnet, D., Yang, Y., Peterson, J.M., Ghosh, B., Chaerkady, R., Leach, S.D., Marchionni, L.*, et al.* (2012). Regulation of Lipid Metabolism by Dicer Revealed through SILAC Mice. J Proteome Res *11*, 2193-2205.

Huntzinger, E., Kuzuoglu-Ozturk, D., Braun, J.E., Eulalio, A., Wohlbold, L., and Izaurralde, E. (2013). The interactions of GW182 proteins with PABP and deadenylases are required for both translational repression and degradation of miRNA targets. Nucleic Acids Res *41*, 978-994.

Isakova, A., Fehlmann, T., Keller, A., and Quake, S.R. (2020). A mouse tissue atlas of small noncoding RNA. Proceedings of the National Academy of Sciences of the United States of America *117*, 25634-25645.

Izaurralde, E. (2015). GENE REGULATION. Breakers and blockers-miRNAs at work. Science *349*, 380-382.

Jee, D., Yang, J.S., Park, S.M., Farmer, D.T., Wen, J., Chou, T., Chow, A., McManus, M.T., Kharas, M.G., and Lai, E.C. (2018). Dual Strategies for Argonaute2-Mediated Biogenesis of Erythroid miRNAs Underlie Conserved Requirements for Slicing in Mammals. Molecular cell *69*, 265-278 e266.

JnBaptiste, C.K., Gurtan, A.M., Thai, K.K., Lu, V., Bhutkar, A., Su, M.J., Rotem, A., Jacks, T., and Sharp, P.A. (2017). Dicer loss and recovery induce an oncogenic switch driven by transcriptional activation of the oncofetal Imp1-3 family. Genes & development *31*, 674-687.

Kaneko, H., Dridi, S., Tarallo, V., Gelfand, B.D., Fowler, B.J., Cho, W.G., Kleinman, M.E., Ponicsan, S.L., Hauswirth, W.W., Chiodo, V.A.*, et al.* (2011). DICER1 deficit induces Alu RNA toxicity in age-related macular degeneration. Nature *471*, 325-330.

Kanellopoulou, C., Muljo, S.A., Kung, A.L., Ganesan, S., Drapkin, R., Jenuwein, T., Livingston, D.M., and Rajewsky, K. (2005). Dicer-deficient mouse embryonic stem cells are defective in differentiation and centromeric silencing. Genes & development *19*, 489-501.

Kim, S.Y., and Volsky, D.J. (2005). PAGE: Parametric analysis of gene set enrichment. Bmc Bioinformatics *6*.

Kim, Y.K., Kim, B., and Kim, V.N. (2016). Re-evaluation of the roles of DROSHA, Export in 5, and DICER in microRNA biogenesis. Proceedings of the National Academy of Sciences of the United States of America *113*, E1881-1889.

Kobayashi, T., Papaioannou, G., Mirzamohammadi, F., Kozhemyakina, E., Zhang, M., Blelloch, R., and Chong, M.W. (2015). Early postnatal ablation of the microRNA-processing enzyme, Drosha, causes chondrocyte death and impairs the structural integrity of the articular cartilage. Osteoarthritis Cartilage *23*, 1214-1220.

Koralov, S.B., Muljo, S.A., Galler, G.R., Krek, A., Chakraborty, T., Kanellopoulou, C., Jensen, K., Cobb, B.S., Merkenschlager, M., Rajewsky, N.*, et al.* (2008). Dicer ablation affects antibody diversity and cell survival in the B lymphocyte lineage. Cell *132*, 860-874.

Kozomara, A., Birgaoanu, M., and Griffiths-Jones, S. (2019). miRBase: from microRNA sequences to function. Nucleic Acids Research *47*, D155-D162.

Kumar, M.S., Lu, J., Mercer, K.L., Golub, T.R., and Jacks, T. (2007). Impaired microRNA processing enhances cellular transformation and tumorigenesis. Nature genetics *39*, 673-677.

La Rocca, G., Olejniczak, S.H., Gonzalez, A.J., Briskin, D., Vidigal, J.A., Spraggon, L., DeMatteo, R.G., Radler, M.R., Lindsten, T., Ventura, A.*, et al.* (2015). In vivo, Argonaute-bound microRNAs exist predominantly in a reservoir of low molecular weight complexes not associated with mRNA. Proceedings of the National Academy of Sciences of the United States of America *112*, 767-772.

Lazzaretti, D., Tournier, I., and Izaurralde, E. (2009). The C-terminal domains of human TNRC6A, TNRC6B, and TNRC6C silence bound transcripts independently of Argonaute proteins. Rna *15*, 1059-1066.

Lee, R.C., Feinbaum, R.L., and Ambros, V. (1993). The C. elegans heterochronic gene lin-4 encodes small RNAs with antisense complementarity to lin-14. Cell *75*, 843-854.

Leung, A.K., and Sharp, P.A. (2010). MicroRNA functions in stress responses. Molecular cell *40*, 205-215.

Lian, S.L., Li, S.Q., Abadal, G.X., Pauley, B.A., Fritzler, M.J., and Chan, E.K.L. (2009). The C-terminal half of human Ago2 binds to multiple GW-rich regions of GW182 and requires GW182 to mediate silencing. Rna *15*, 804-813.

Liu, J.D., Carmell, M.A., Rivas, F.V., Marsden, C.G., Thomson, J.M., Song, J.J., Hammond, S.M., Joshua-Tor, L., and Hannon, G.J. (2004). Argonaute2 is the catalytic engine of mammalian RNAi. Science *305*, 1437-1441.

Liu, N., Bezprozvannaya, S., Williams, A.H., Qi, X.X., Richardson, J.A., Bassel-Duby, R., and Olson, E.N. (2008). microRNA-133a regulates cardiomyocyte proliferation and suppresses smooth muscle gene expression in the heart. Genes & Development *22*, 3242-3254.

Liu, Z., Johnson, S.T., Zhang, Z., and Corey, D.R. (2019). Expression of TNRC6 (GW182) Proteins Is Not Necessary for Gene Silencing by Fully Complementary RNA Duplexes. Nucleic Acid Ther *29*, 323-334.

Love, M.I., Huber, W., and Anders, S. (2014). Moderated estimation of fold change and dispersion for RNA-seq data with DESeq2. Genome Biol *15*.

Macias, S., Cordiner, R.A., Gautier, P., Plass, M., and Caceres, J.F. (2015). DGCR8 Acts as an Adaptor for the Exosome Complex to Degrade Double-Stranded Structured RNAs. Molecular cell *60*, 873-885.

McKenna, L.B., Schug, J., Vourekas, A., McKenna, J.B., Bramswig, N.C., Friedman, J.R., and Kaestner, K.H. (2010). MicroRNAs control intestinal epithelial differentiation, architecture, and barrier function. Gastroenterology *139*, 1654-1664, 1664 e1651.

Mendell, J.T., and Olson, E.N. (2012). MicroRNAs in stress signaling and human disease. Cell *148*, 1172-1187.

Michelini, F., Pitchiaya, S., Vitelli, V., Sharma, S., Gioia, U., Pessina, F., Cabrini, M., Wang, Y., Capozzo, I., Iannelli, F.*, et al.* (2017). Damage-induced lncRNAs control the DNA damage response through interaction with DDRNAs at individual double-strand breaks. Nat Cell Biol *19*, 1400-1411.

Ng, A.P., and Alexander, W.S. (2017). Haematopoietic stem cells: past, present and future. Cell Death Discov *3*, 17002.

Nishihara, T., Zekri, L., Braun, J.E., and Izaurralde, E. (2013). miRISC recruits decapping factors to miRNA targets to enhance their degradation. Nucleic Acids Research *41*, 8692-8705.

Niwa, H., Yamamura, K., and Miyazaki, J. (1991). Efficient selection for high-expression transfectants with a novel eukaryotic vector. Gene *108*, 193-199.

Oikawa, S., Lee, M., and Akimoto, T. (2019a). Conditional Deletion of Dicer in Adult Mice Impairs Skeletal Muscle Regeneration. Int J Mol Sci *20*.

Oikawa, S., Lee, M., Motohashi, N., Maeda, S., and Akimoto, T. (2019b). An inducible knockout of Dicer in adult mice does not affect endurance exercise-induced muscle adaptation. Am J Physiol-Cell Ph *316*, C285-C292.

Okamura, K., Hagen, J.W., Duan, H., Tyler, D.M., and Lai, E.C. (2007). The mirtron pathway generates microRNA-class regulatory RNAs in Drosophila. Cell *130*, 89-100.

Okamura, K., and Lai, E.C. (2008). Endogenous small interfering RNAs in animals. Nat Rev Mol Cell Biol *9*, 673-678.

1179 Okayasu, I., Hatakeyama, S., Yamada, M., Ohkusa, T., Inagaki, Y., and Nakaya, R. (1990). A Novel
1180 Method in the Induction of Reliable Experimental Acute and Chronic Ulcerative-Colitis in Mice.
1181 Gastroenterology *98*, 694-702.

1182 Olejniczak, S.H., La Rocca, G., Gruber, J.J., and Thompson, C.B. (2013). Long-lived microRNA-
1183 Argonaute complexes in quiescent cells can be activated to regulate mitogenic responses. Proceedings
1184 of the National Academy of Sciences of the United States of America *110*, 157-162.

1185 Park, C.Y., Choi, Y.S., and McManus, M.T. (2010). Analysis of microRNA knockouts in mice. Hum Mol
1186 Genet *19*, R169-R175.

1187 Patrick, D.M., Zhang, C.C., Tao, Y., Yao, H., Qi, X., Schwartz, R.J., Jun-Shen Huang, L., and Olson,
1188 E.N. (2010). Defective erythroid differentiation in miR-451 mutant mice mediated by 14-3-3zeta. Genes
1189 & development *24*, 1614-1619.

1190 Pfaff, J., Hennig, J., Herzog, F., Aebersold, R., Sattler, M., Niessing, D., and Meister, G. (2013).
1191 Structural features of Argonaute-GW182 protein interactions. Proceedings of the National Academy of
1192 Sciences of the United States of America *110*, E3770-E3779.

1193 Premsrirut, P.K., Dow, L.E., Kim, S.Y., Camiolo, M., Malone, C.D., Miething, C., Scuoppo, C., Zuber, J.,
1194 Dickins, R.A., Kogan, S.C.*, et al.* (2011). A Rapid and Scalable System for Studying Gene Function in
1195 Mice Using Conditional RNA Interference. Cell *145*, 145-158.

1196 Rehwinkel, J., Behm-Ansmant, I., Gatfield, D., and Izaurralde, E. (2005). A crucial role for GW182 and
1197 the DCP1:DCP2 decapping complex in miRNA-mediated gene silencing. Rna *11*, 1640-1647.

1198 Reinhart, B.J., Slack, F.J., Basson, M., Pasquinelli, A.E., Bettinger, J.C., Rougvie, A.E., Horvitz, H.R.,
1199 and Ruvkun, G. (2000). The 21-nucleotide let-7 RNA regulates developmental timing in Caenorhabditis
1200 elegans. Nature *403*, 901-906.

1201 Ruby, J.G., Jan, C.H., and Bartel, D.P. (2007). Intronic microRNA precursors that bypass Drosha
1202 processing. Nature *448*, 83-86.

1203 Schirle, N.T., Sheu-Gruttadauria, J., and MacRae, I.J. (2014). Structural basis for microRNA targeting.
1204 Science *346*, 608-613.

1205 Sheu-Gruttadauria, J., and MacRae, I.J. (2018). Phase Transitions in the Assembly and Function of
1206 Human miRISC. Cell *173*, 946-957 e916.

1207 Song, J.L., Stoeckius, M., Maaskola, J., Friedlander, M., Stepicheva, N., Juliano, C., Lebedeva, S.,
1208 Thompson, W., Rajewsky, N., and Wessel, G.M. (2012). Select microRNAs are essential for early
1209 development in the sea urchin. Dev Biol *362*, 104-113.

1210 Song, M.S., and Rossi, J.J. (2017). Molecular mechanisms of Dicer: endonuclease and enzymatic
1211 activity. Biochem J *474*, 1603-1618.

1212 Stein, P., Rozhkov, N.V., Li, F., Cardenas, F.L., Davydenko, O., Vandivier, L.E., Gregory, B.D.,
1213 Hannon, G.J., and Schultz, R.M. (2015). Essential Role for endogenous siRNAs during meiosis in
1214 mouse oocytes. PLoS genetics *11*, e1005013.

1215 Tam, O.H., Aravin, A.A., Stein, P., Girard, A., Murchison, E.P., Cheloufi, S., Hodges, E., Anger, M.,
1216 Sachidanandam, R., Schultz, R.M*., et al.* (2008). Pseudogene-derived small interfering RNAs regulate
1217 gene expression in mouse oocytes. Nature *453*, 534-538.

1218 Till, S., Lejeune, E., Thermann, R., Bortfeld, M., Hothorn, M., Enderle, D., Heinrich, C., Hentze, M.W.,
1219 and Ladurner, A.G. (2007). A conserved motif in Argonaute-interacting proteins mediates functional
1220 interactions through the Argonaute PIWI domain. Nature Structural & Molecular Biology *14*, 897-903.

1221 Treiber, T., Treiber, N., and Meister, G. (2019). Regulation of microRNA biogenesis and its crosstalk
1222 with other cellular pathways. Nat Rev Mol Cell Biol *20*, 5-20.

1223 Turturici, G., La Fiora, V., Terenzi, A., Barone, G., and Cavalieri, V. (2018). Perturbation of
1224 Developmental Regulatory Gene Expression by a G-Quadruplex DNA Inducer in the Sea Urchin
1225 Embryo. Biochemistry-Us *57*, 4391-4394.

1226 van Rooij, E., Sutherland, L.B., Qi, X., Richardson, J.A., Hill, J., and Olson, E.N. (2007). Control of
1227 stress-dependent cardiac growth and gene expression by a microRNA. Science *316*, 575-579.

1228 Vechetti, I.J., Wen, Y., Chaillou, T., Murach, K.A., Alimov, A.P., Figueiredo, V.C., Dal-Pai-Silva, M., and
1229 McCarthy, J.J. (2019). Life-long reduction in myomiR expression does not adversely affect skeletal
1230 muscle morphology. Sci Rep-Uk *9*.

1231 Ventura, A., Young, A.G., Winslow, M.M., Lintault, L., Meissner, A., Erkeland, S.J., Newman, J.,
1232 Bronson, R.T., Crowley, D., Stone, J.R*., et al.* (2008). Targeted deletion reveals essential and
1233 overlapping functions of the miR-17 through 92 family of miRNA clusters. Cell *132*, 875-886.

1234 Wang, Y.M., Medvid, R., Melton, C., Jaenisch, R., and Blelloch, R. (2007). DGCR8 is essential for
1235 microRNA biogenesis and silencing of embryonic stem cell self-renewal. Nature genetics *39*, 380-385.

1236 Wienholds, E., Koudijs, M.J., van Eeden, F.J., Cuppen, E., and Plasterk, R.H. (2003). The microRNA-
1237 producing enzyme Dicer1 is essential for zebrafish development. Nature genetics *35*, 217-218.

1238 Wightman, B., Ha, I., and Ruvkun, G. (1993). Posttranscriptional regulation of the heterochronic gene
1239 lin-14 by lin-4 mediates temporal pattern formation in C. elegans. Cell *75*, 855-862.

1240 Williams, A.H., Valdez, G., Moresi, V., Qi, X.X., McAnally, J., Elliott, J.L., Bassel-Duby, R., Sanes, J.R.,
1241 and Olson, E.N. (2009). MicroRNA-206 Delays ALS Progression and Promotes Regeneration of
1242 Neuromuscular Synapses in Mice. Science *326*, 1549-1554.

1243 Yang, J.S., and Lai, E.C. (2011). Alternative miRNA biogenesis pathways and the interpretation of core
1244 miRNA pathway mutants. Molecular cell *43*, 892-903.

Yekta, S., Shih, I.H., and Bartel, D.P. (2004). MicroRNA-directed cleavage of HOXB8 mRNA. Science *304*, 594-596.

Zeng, Y., Yi, R., and Cullen, B.R. (2003). MicroRNAs and small interfering RNAs can inhibit mRNA expression by similar mechanisms. Proceedings of the National Academy of Sciences of the United States of America *100*, 9779-9784.

Zielezinski, A., and Karlowski, W.M. (2015). Early origin and adaptive evolution of the GW182 protein family, the key component of RNA silencing in animals. RNA Biol *12*, 761-770.

Zipprich, J.T., Bhattacharyya, S., Mathys, H., and Filipowicz, W. (2009). Importance of the C-terminal domain of the human GW182 protein TNRC6C for translational repression. Rna *15*, 781-793.

Figure Supplement Legends

Figure 1- figure supplement 1. (**a**) HCTT116 cells transduced with retroviral vectors expressing a doxycycline-inducible T6B or $T6B^{Mut}$ transgene (FH-T6B-YFP) were cultured in the presence of doxycycline for 48h. Whole cells lysates were probed with an anti-HA antibody. (**b**) Lysates from (a) were immunoprecipitated with the indicated antibodies and blotted against AGO2, FH-T6B-YFP (anti-HA) and GAPDH. Note that the T6B fusion protein, but not its mutant version ($T6B^{Mut}$), binds to AGO proteins. Lower panel. Aminoacid sequence of the T6B and $T6B^{Mut}$ fusion proteins. Both T6B versions have HA and FLAG tags at the N termini and are fused to the yellow fluorescent protein (YFP) at the C-termini. In $T6B^{Mut}$, all Tryptophan residues (red) are mutated to Alanine to prevent interaction with AGO proteins. Blue, FLAG-tag; light blue, HA-tag; bold black, T6B; green, YFP.

Figure 1- figure supplement 2. Size exclusion chromatography was performed on whole cell lysates from MEFs transduced with retroviral vectors expressing a doxycycline-inducible T6B or $T6B^{Mut}$ transgene and cultured in presence of doxycycline for 48h. Eluted fractions were probed with the anti-AGO2 or anti-HA antibodies to determine the elution profile of AGO2 and T6B, respectively.

Figure 2 - figure supplement 1 (**a**) Two independent targeted ES clones were cultured in the presence or absence of doxycycline for 48h and examined by epifluorescence microscopy to detect FH-T6B-YFP expression. The same exposure was used for all images. Bright field images are also shown for each clone. (**b**) Whole cell lysates from the clones shown in (a) were probed with an anti-HA antibody to detect expression of the T6B fusion protein.

Figure 2 - figure supplement 2. Immunofluorescence imaging using a YFP-specific antibody, showing T6B expression in a panel of tissues of adult $R26^{T6B}$ mice (second column) and CAG^{T6B} mice (third column) fed doxycycline-containing diet for 7 days. Tissues from $R26^{CTL}$ (first column) mice fed doxycycline-containing diet for 7 days were included as negative controls.

Figure 2 - figure supplement 3. Total extracts from the colon of $R26^{T6B}$ mice kept on doxycycline-containing diet for 1 week were immunoprecipitated using an anti-YFP antibody and probed with the indicated antibodies to measure the interaction between the T6B fusion protein and AGO2 *in vivo*. An anti-HA antibody was used to detect T6B.

Figure 2 - figure supplement 4. SEC fractionation followed by Western blotting of total extracts from the liver and large intestine of control and $R26^{T6B}$ mice treated with doxycycline-containing chow for 7 days. The shift of AGO2 from high molecular weight to low molecular weight complexes confirms disruption of the miRISC.

Figure 3 - figure supplement 1. (**a**) Litter obtained by c-section from a pregnant *Rosa26*$^{rtTA/rtTA}$; *Col1a1*$^{T6B/+}$ female crossed to a *Rosa26*$^{rtTA/rtTA}$*; Col1a1*$^{T6B/+}$ male and maintained on doxycycline from d.p.c. 13.5 to d.p.c. 18.5. (**b**) Pups from (a) were weighted and genotyped and the results plotted. p-value: two-tailed unpaired t test.

Figure 3 - figure supplement 2. Immunofluorescence imaging of the small and large intestine of $R26^{T6B}$ and $R26^{CTL}$ mice kept on doxycycline diet for a month. An antibody against YFP was used to detect the T6B fusion protein.

Figure 3 - figure supplement 3. Sections from the colon and small intestine sections of $R26^{T6B}$ and control mice kept on doxycycline-containing diet for 2 months were probed by IHC with an anti-Ki67 antibody.

Figure 3 - figure supplement 4. Detection of goblet cells by staining of acidic and neutral mucins in intestine sections from $R26^{T6B}$ and control mice kept on doxycycline diet for 2 months. Neutral mucins are stained with periodic acid-Shiff whereas acidic mucins are stained with Alcian blue.

Figure 3 - figure supplement 5. Body weight of $R26^{T6B}$ (n = 5) and control (n = 8) female mice was assessed after 2 month-administration of doxycycline-containing chow. ns, not significant (p = 0. 6264, unpaired t test).

Figure 3 - figure supplement 6. Complete blood counts (CBC) of whole blood from $R26^{T6B}$ and $R26^{CTL}$ mice taken after 3 weeks on doxycycline. Abbreviations are as follows: RBC = red blood cell count, HGB = hemoglobin, HCT = hematocrit, MCV = mean corpuscular volume, MCH = mean cell hemoglobin, RDW = red cell distribution width, RET = reticulocyte count, WBC = white blood cell count, PLT = platelet count.

Figure 3 - figure supplement 7. Representative flow cytometry plots showing the gating strategy for the identification of hematopoietic stem and progenitor cells from whole bone marrow harvested from $R26^{T6B}$ and $R26^{CTL}$ mice maintained on doxycycline diet for 3 weeks. LT-HSC: Lin- Kit+ Sca1+ CD150+

CD48-, ST-HSC: Lin- Kit+ Sca1+ CD150- CD48-, MPP2: Lin- Kit+ Sca1+ CD150+ CD48+, MPP3/4: Lin- Kit+ Sca1+ CD150- CD48+.

Figure 3 - figure supplement 8. Representative flow cytometry plots showing the gating strategy for the identification of B cell lineage populations from whole bone marrow harvested from $R26^{T6B}$ and $R26^{CTL}$ mice maintained on doxycycline diet for 3 weeks. Pro-B: B220+CD19+IgD-IgM-CD25-Kit+, Pre-B: B220+CD19+IgD-IgM-CD25+, Imm B: B220+CD19+IgD-IgM+, Mat B: B220+CD19+IgD+IgM+/lo.

Figure 4 - figure supplement 1. Bar plots showing measurement of colon length, aggregated length of ulcers, percentage of colon with ulcers, area of ulcers, number of immune nodules and the area of immune nodules performed on H&E longitudinal sections of colon from $R26^{CTL}$ and $R26^{T6B}$ mice 5 days post-DSS treatment. Measurements of these parameters were obtained using OMERO (https://www.openmicroscopy.org/omero/) and used to estimate the extent of damage and colitis induced by DSS treatment. Plots show that no significant differences between $R26^{CTL}$ and $R26^{T6B}$ mice were observed, suggesting that both groups experienced similar level of DSS-induced colitis.

Figure 4 - figure supplement 2. Representative immunohistochemistry image showing Ki67 signal in control mice (n = 3) 5 days after DSS treatment was discontinued. The presence of highly proliferating cells indicates residual dysplasia.

Figure 6 - figure supplement 1. Body weight of CAG^{T6B} and control mice maintained on doxycycline for up to 45 days was assessed the day on which euthanasia was performed. n = 8 (4 females and 4 males) for each genotype (age and sex matched). Mice were kept on doxycycline diet throughout the duration of the experiment and control mice were euthanized at day 45. P-values: unpaired t-test.

Figure 6 - figure supplement 2. Representative H&E staining showing vasculitis of the pulmonary veins as revealed by inflammatory immune cell infiltration of the vessel wall (arrows).

Figure 6 - figure supplement 3. T6B blocks miRNA activity in sea urchins and zebrafish. (**a**) Left panel: Representative examples of Mediterranean sea urchin (*P. lividus*) zygotes injected with 1 pg of *in vitro*-transcribed mRNA coding for either T6B or $T6B^{Mut}$ proteins and observed under DIC optics at 48 hours post-fertilization. Both embryos are oriented in a vegetal view. T6B-expressing embryos displayed severe developmental aberrations ranging from the failure to form a proper archenteron and skeletal structures, to overall delay in development and embryonic lethality. By contrast, control $T6B^{Mut}$-expressing embryos observed at the same developmental stage went through embryogenesis normally and exhibited the characteristic easel-like shape of the echinoid pluteus larva. Right panel: quantitative PCR showing dysregulation of territorial marker genes involved in the developmental gene regulatory network of the sea urchin (Cavalieri and Spinelli, 2015a) (Cavalieri and Spinelli, 2015b) upon T6B expression. Data are indicated as fold difference in transcript abundance with respect to control $T6B^{Mut}$-expressing embryos at the same stage of development. The gray region represents changes in mRNA abundance corresponding to less than 3-fold difference, while error bars are standard errors for the qPCR replicates. Abbreviations: PMCs, primary mesenchyme cells; SMCs, secondary mesenchyme cells. (**b**) Zebrafish (*Danio rerio*) fertilized eggs were injected with 75 pg of *in vitro*-transcribed mRNA coding for either T6B or $T6B^{Mut}$ fusion proteins. While $T6B^{Mut}$-expressing embryos developed normally, the majority of T6B-expressing embryos underwent severe developmental defects.

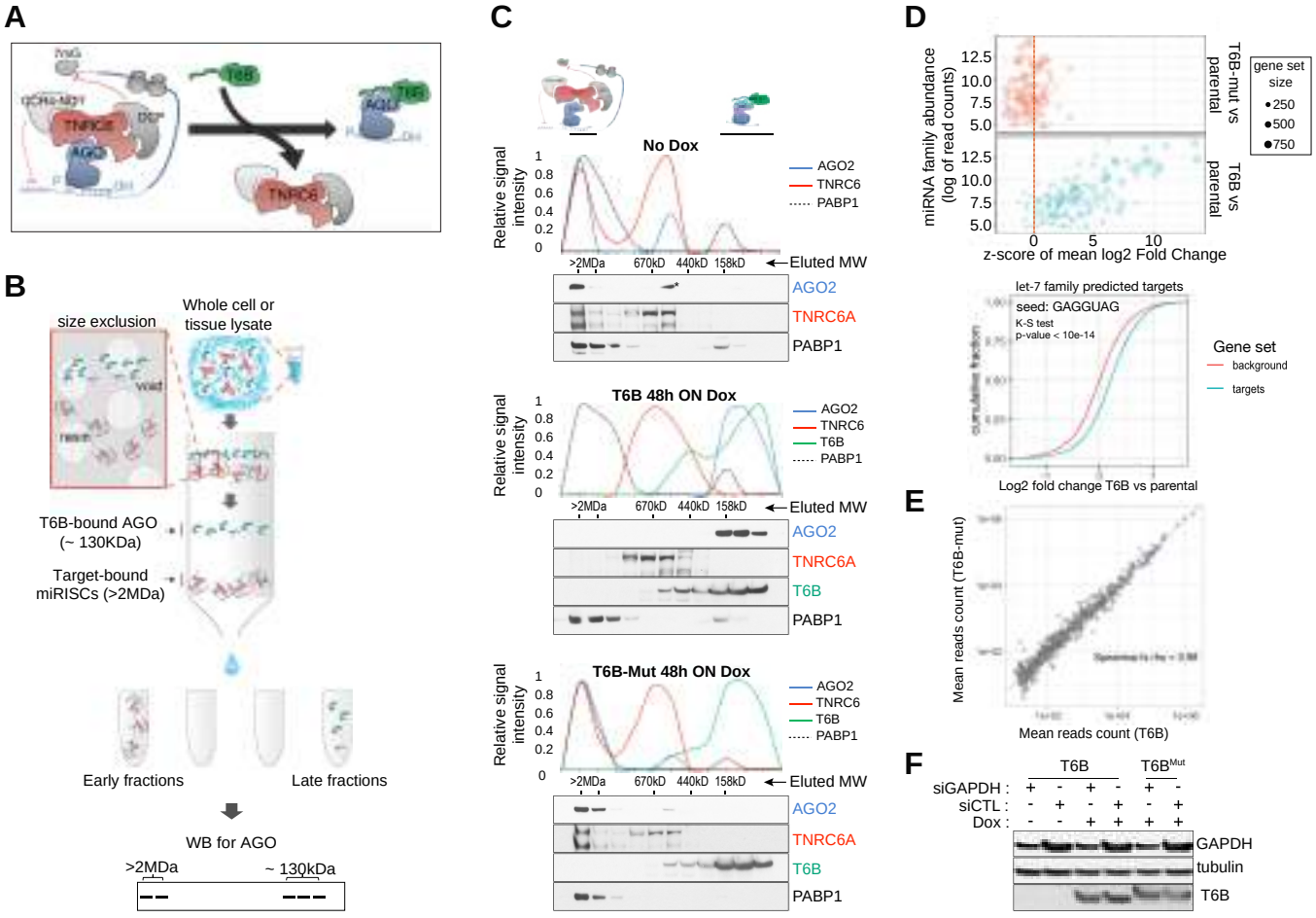
A
T6B
AGO
TNRC6
B
size exclusion
Whole cell or tissue lysate
T6B-bound AGO (~ 130KDa)
Target-bound miRISCs (>2MDa)
Early fractions
Late fractions
WB for AGO
>2MDa
~ 130kDa
C
No Dox
T6B 48h ON Dox
T6B-Mut 48h ON Dox
Relative signal intensity
>2MDa
670kD
440kD
158kD
Eluted MW
AGO2
TNRC6
TNRC6A
T6B
PABP1
D
miRNA family abundance (log of read counts)
T6B-mut vs parental
T6B vs parental
gene set size
250
500
750
z-score of mean log2 Fold Change
let-7 family predicted targets
seed: GAGGUAG
K-S test
p-value < 10e-14
Gene set
background
targets
Log2 fold change T6B vs parental
E
Mean reads count (T6B-mut)
Mean reads count (T6B)
F
T6B
T6B^Mut
siGAPDH :
siCTL :
Dox :
GAPDH
tubulin
T6B

Figure 1

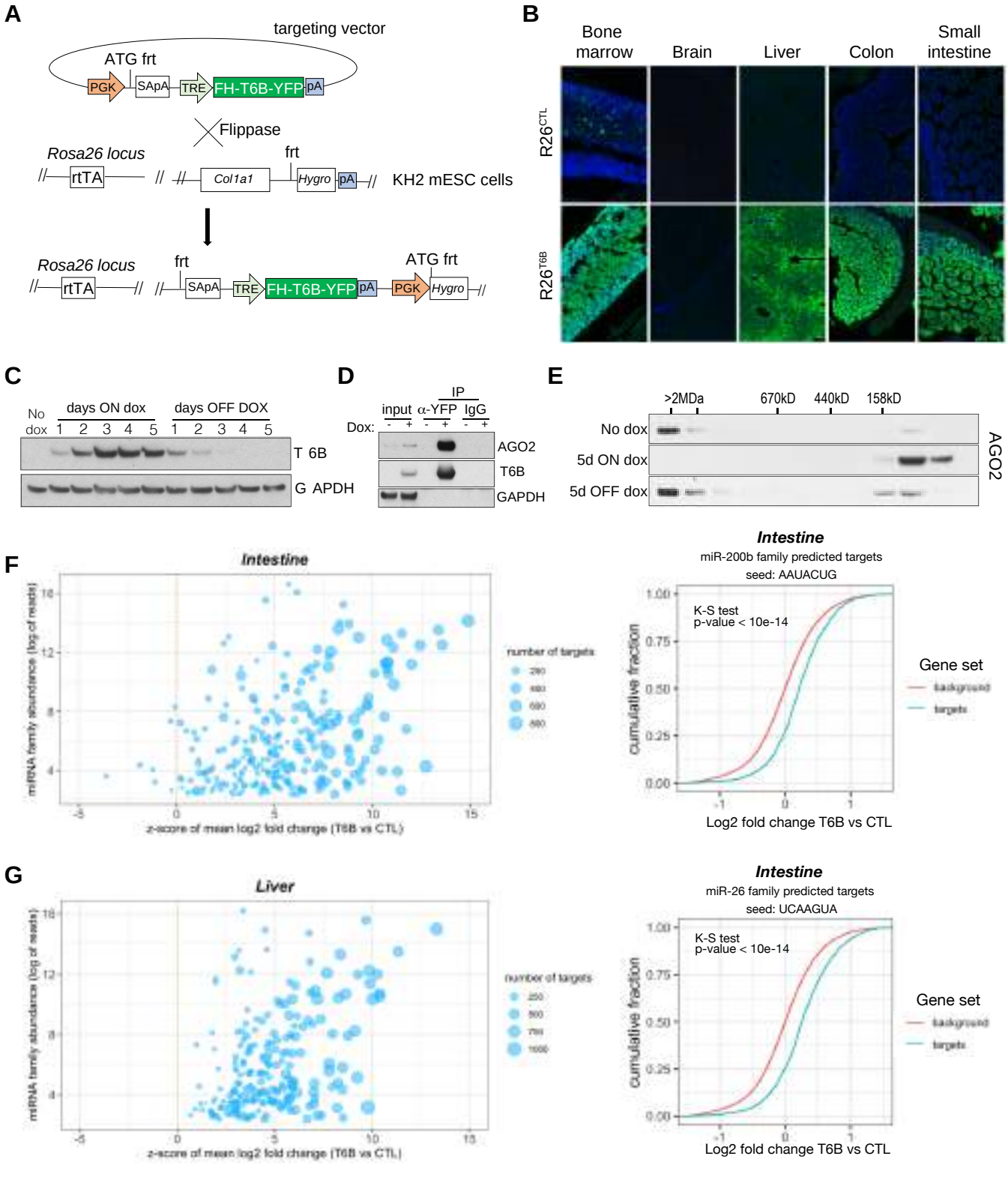
A
targeting vector
ATG frt
PGK
SApA
TRE
FH-T6B-YFP
pA
Flippase
Rosa26 locus
rtTA
frt
Col1a1
Hygro
KH2 mESC cells
ATG frt
B
Bone marrow
Brain
Liver
Colon
Small intestine
R26CTL
R26T6B
C
No dox
days ON dox
days OFF DOX
T 6B
G APDH
D
IP
input
α-YFP
IgG
Dox:
AGO2
T6B
GAPDH
E
>2MDa
670kD
440kD
158kD
No dox
5d ON dox
5d OFF dox
AGO2
F
Intestine
miRNA family abundance (log of reads)
z-score of mean log2 fold change (T6B vs CTL)
number of targets
Intestine
miR-200b family predicted targets
seed: AAUACUG
K-S test
p-value < 10e-14
cumulative fraction
Log2 fold change T6B vs CTL
Gene set
background
targets
G
Liver
miRNA family abundance (log of reads)
z-score of mean log2 fold change (T6B vs CTL)
number of targets
Intestine
miR-26 family predicted targets
seed: UCAAGUA
K-S test
p-value < 10e-14
cumulative fraction
Log2 fold change T6B vs CTL
Gene set
background
targets

Figure 2

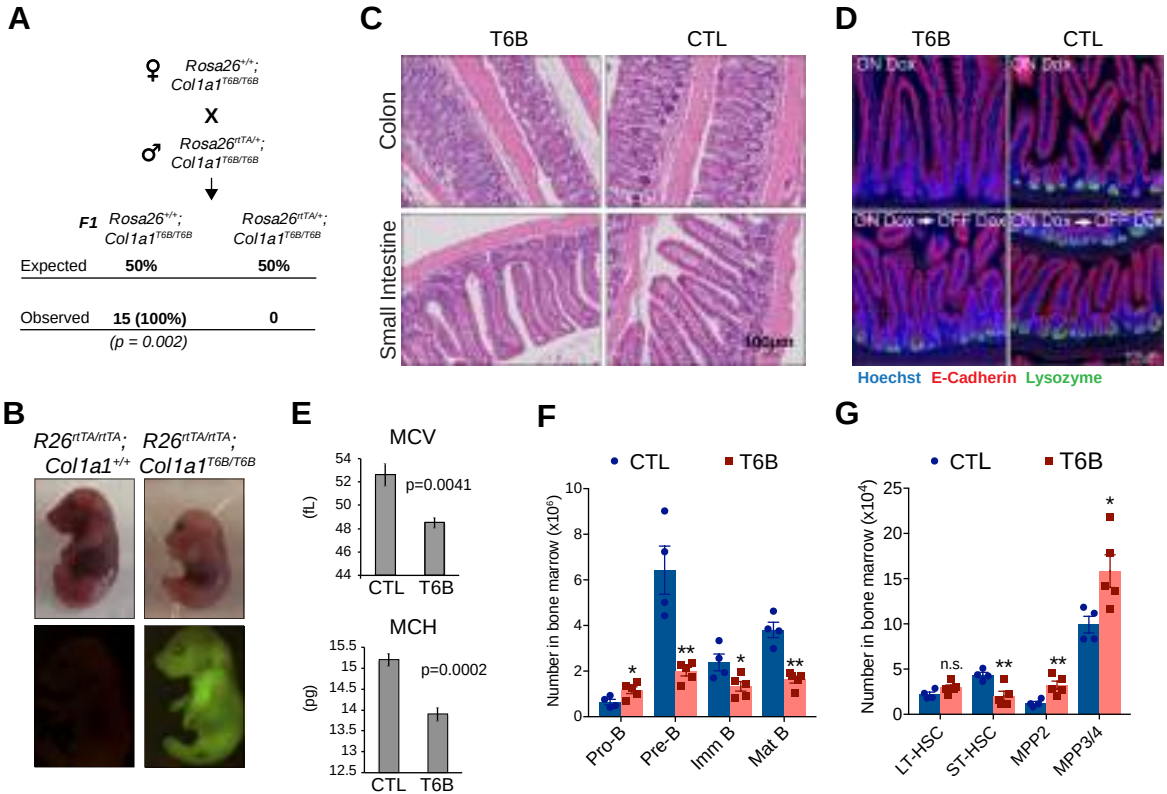
A
♀ Rosa26+/+; Col1a1T6B/T6B
X
♂ Rosa26rtTA/+; Col1a1T6B/T6B
F1 Rosa26+/+; Col1a1T6B/T6B
Rosa26rtTA/+; Col1a1T6B/T6B
Expected 50% 50%
Observed 15 (100%) 0
(p = 0.002)
B
R26rtTA/rtTA; Col1a1+/+
R26rtTA/rtTA; Col1a1T6B/T6B
C
T6B
CTL
Colon
Small Intestine
100µm
D
T6B
CTL
ON Dox
ON Dox → OFF Dox
Hoechst E-Cadherin Lysozyme
E
MCV
(fL)
p=0.0041
CTL T6B
MCH
(pg)
p=0.0002
CTL T6B
F
CTL T6B
Number in bone marrow (x10⁶)
Pro-B Pre-B Imm B Mat B
G
CTL T6B
Number in bone marrow (x10⁴)
n.s.
LT-HSC ST-HSC MPP2 MPP3/4

Figure 3

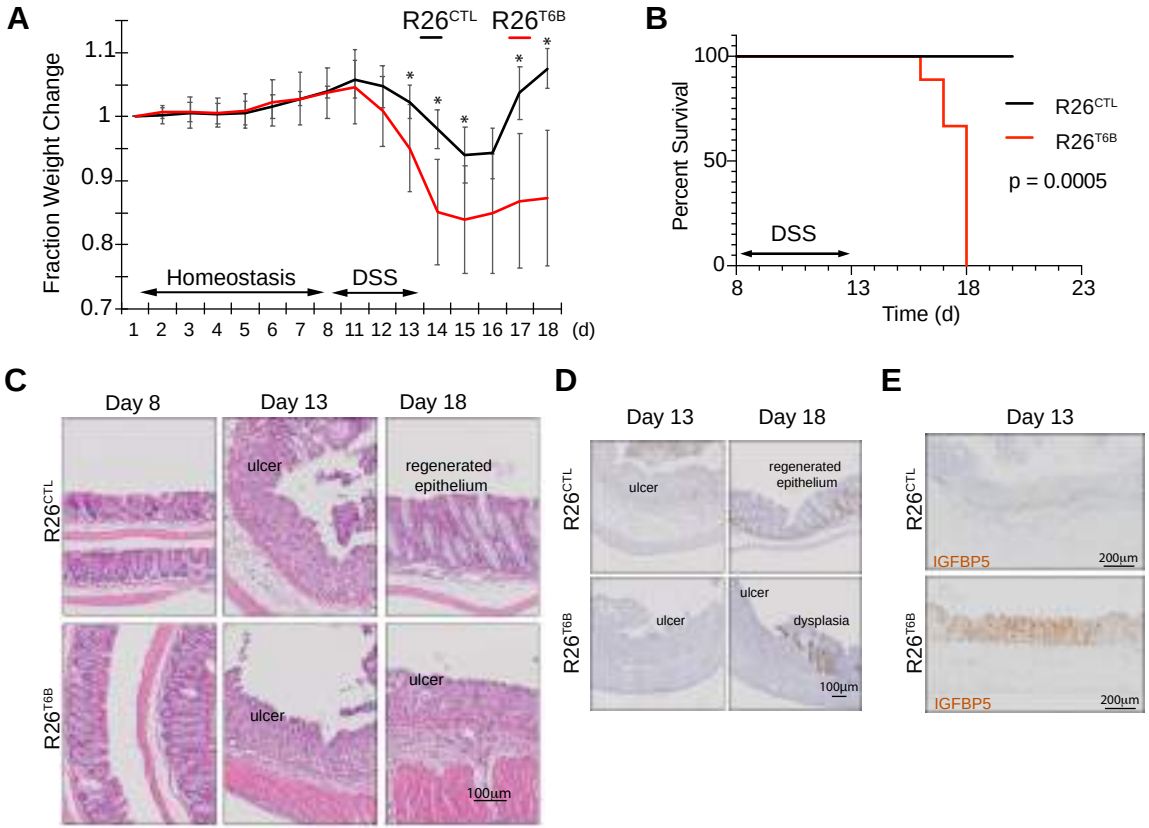
A
R26CTL
R26T6B
Fraction Weight Change
1.1
1
0.9
0.8
0.7
Homeostasis
DSS
1 2 3 4 5 6 7 8 11 12 13 14 15 16 17 18 (d)
B
Percent Survival
100
50
0
DSS
8 13 18 23
Time (d)
R26CTL
R26T6B
p = 0.0005
C
Day 8
Day 13
Day 18
R26CTL
R26T6B
ulcer
regenerated epithelium
ulcer
ulcer
ulcer
100μm
D
Day 13
Day 18
R26CTL
R26T6B
ulcer
regenerated epithelium
ulcer
ulcer
dysplasia
100μm
E
Day 13
R26CTL
R26T6B
IGFBP5
200μm
IGFBP5
200μm

Figure 4

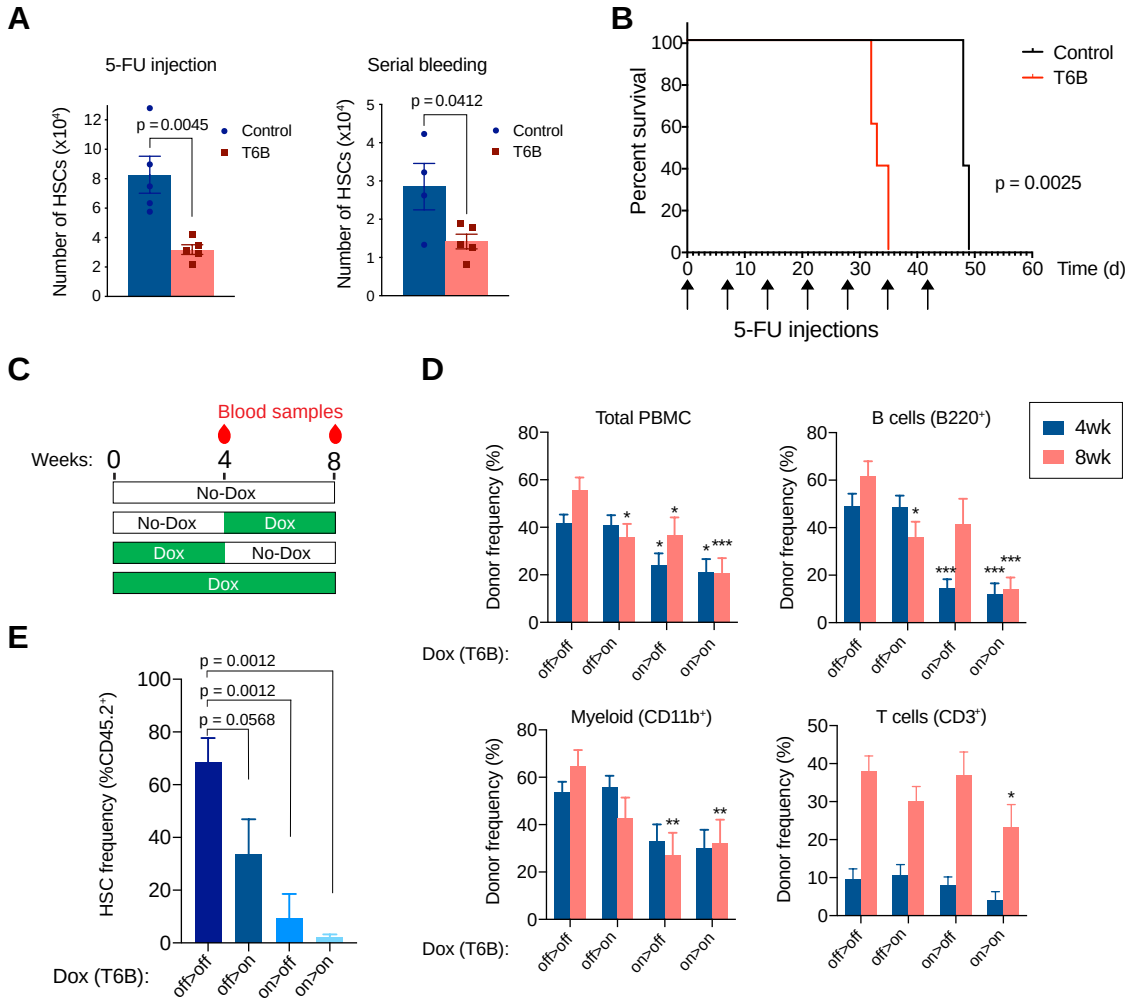
A
5-FU injection
Number of HSCs (x10⁴)
p = 0.0045
Control
T6B
Serial bleeding
Number of HSCs (x10⁴)
p = 0.0412
Control
T6B
B
Percent survival
Control
T6B
p = 0.0025
Time (d)
5-FU injections
C
Blood samples
Weeks: 0 4 8
No-Dox
No-Dox Dox
Dox No-Dox
Dox
D
Total PBMC
B cells (B220⁺)
Myeloid (CD11b⁺)
T cells (CD3⁺)
Donor frequency (%)
4wk
8wk
Dox (T6B):
off>off
off>on
on>off
on>on
E
HSC frequency (%CD45.2⁺)
p = 0.0012
p = 0.0012
p = 0.0568
Dox (T6B):
off>off
off>on
on>off
on>on

Figure 5

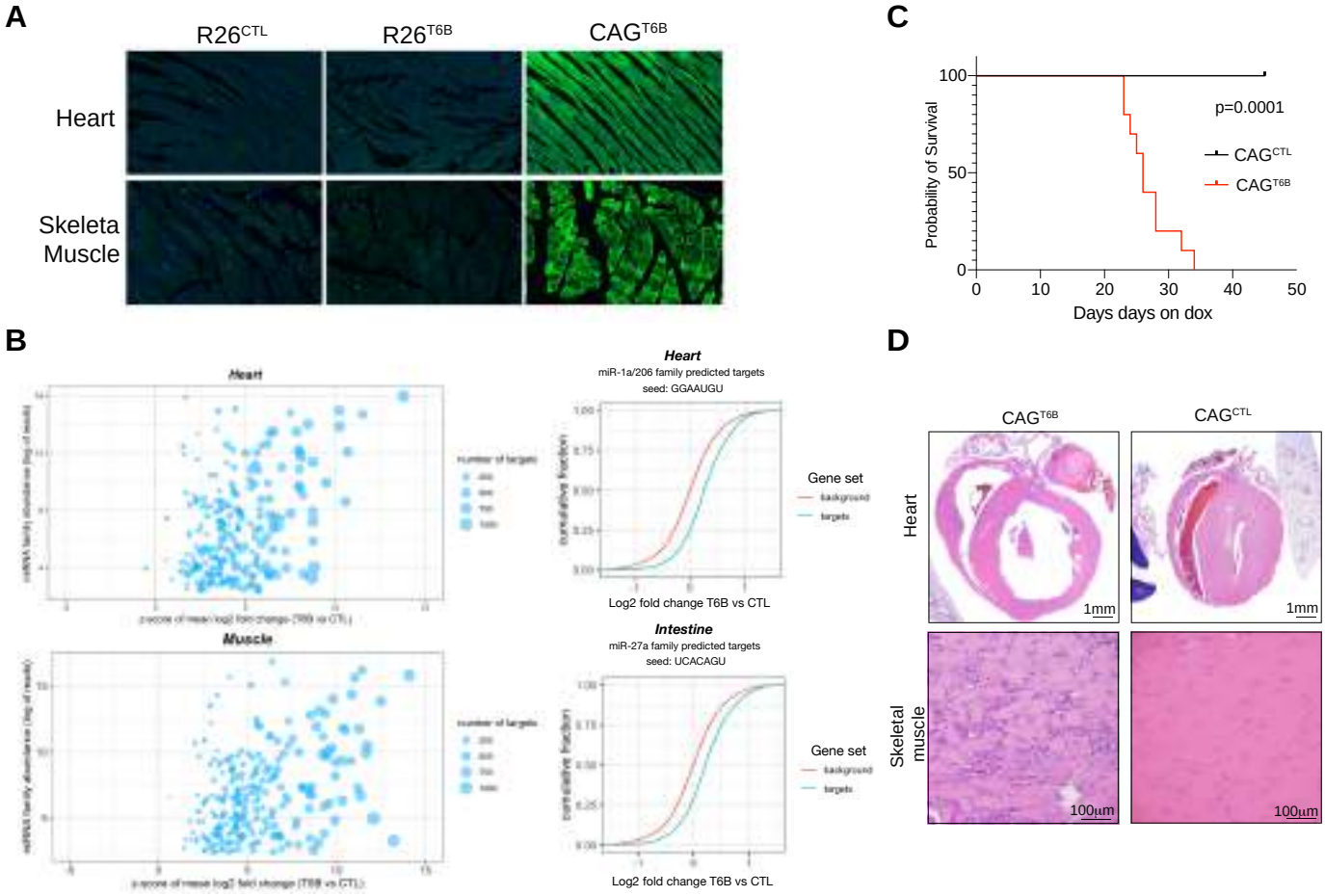
A
R26CTL
R26T6B
CAGT6B
Heart
Skeleta Muscle
C
Probability of Survival
100
50
0
0
10
20
30
40
50
Days days on dox
p=0.0001
CAGCTL
CAGT6B
B
Heart
Muscle
Heart
miR-1a/206 family predicted targets
seed: GGAAUGU
Intestine
miR-27a family predicted targets
seed: UCACAGU
Gene set
background
targets
Log2 fold change T6B vs CTL
D
CAGT6B
CAGCTL
Heart
Skeletal muscle
1mm
100µm

Figure 6

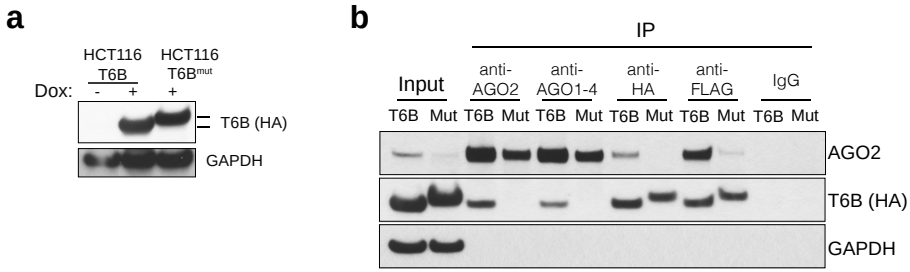

T6B fusion protein sequence:

MDYKDDDDKYPYDVPDYASGR**DCQAVLQTLLSRTDLDPRVLSNTGWGQTQIKQDTVWDIEEVPRPEGKSDKGTEGWESAATQ**
TKNSGGWGDAPSQSNQMKSGWGELVATGSMVSKGEELFTGVVPILVELDGDVNGHKFSVSGEGEGDATYGKLTLKFICTTGKLP
VPWPTLVTTFGYGLQCFARYPDHMKQHDFFKSAMPEGYVQERTIFFKDDGNYKTRAEVKFEGDTLVNRIELKGIDFKEDGNILGH
KLEYNYNSHNVYIMADKQKNGIKVNFKIRHNIEDGSVQLADHYQQNTPIGDGPVLLPDNHYLSYQSALSKDPNEKRDHMVLLEF
VTAAGITLGMDELYK

T6B^{Mut} fusion protein sequence:

MDYKDDDDKYPYDVPDYASGR**DCQAVLQTLLSRTDLDPRVLSNTGAGQTQIKQDTVADIEEVPRPEGKSDKGTEGAESAATQ**
TKNSGGAGDAPSQSNQMKSGAGELVATGSMVSKGEELFTGVVPILVELDGDVNGHKFSVSGEGEGDATYGKLTLKFICTTGKLP
VPWPTLVTTFGYGLQCFARYPDHMKQHDFFKSAMPEGYVQERTIFFKDDGNYKTRAEVKFEGDTLVNRIELKGIDFKEDGNILGH
KLEYNYNSHNVYIMADKQKNGIKVNFKIRHNIEDGSVQLADHYQQNTPIGDGPVLLPDNHYLSYQSALSKDPNEKRDHMVLLEF
VTAAGITLGMDELYK

Figure 1-figure supplement 1

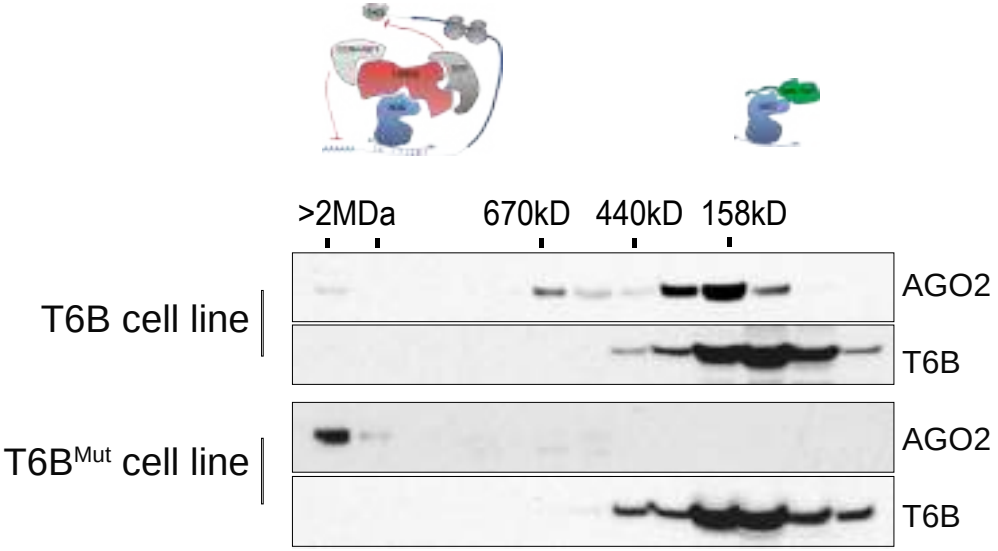

Figure 1-figure supplement 2

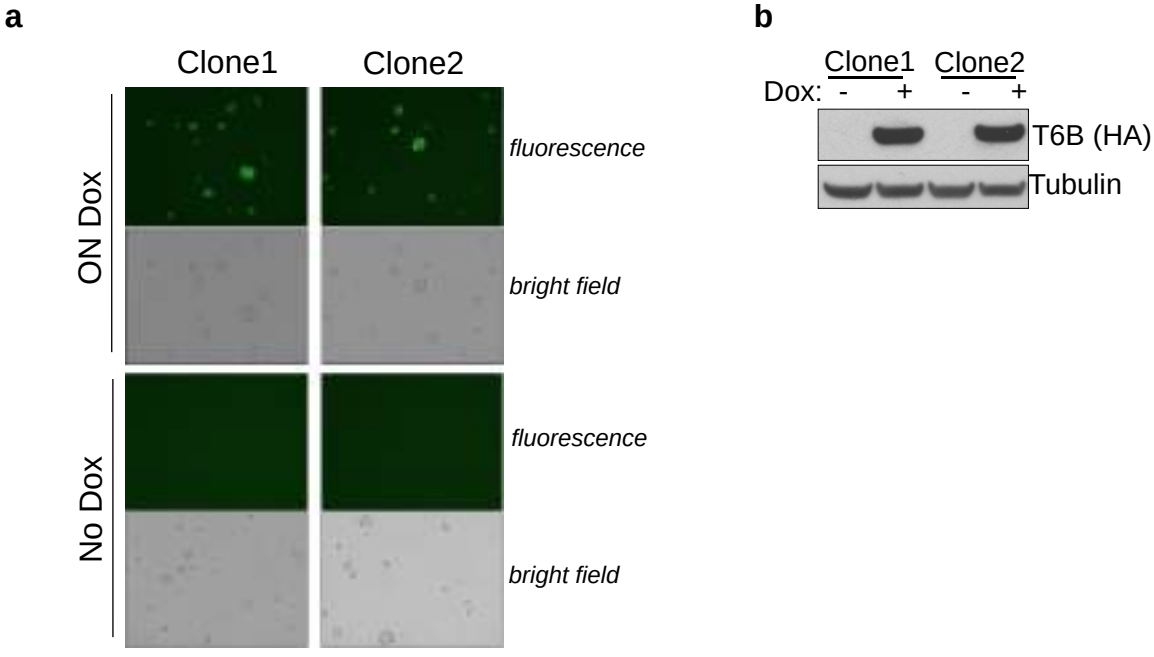

Figure 2-figure supplement 1

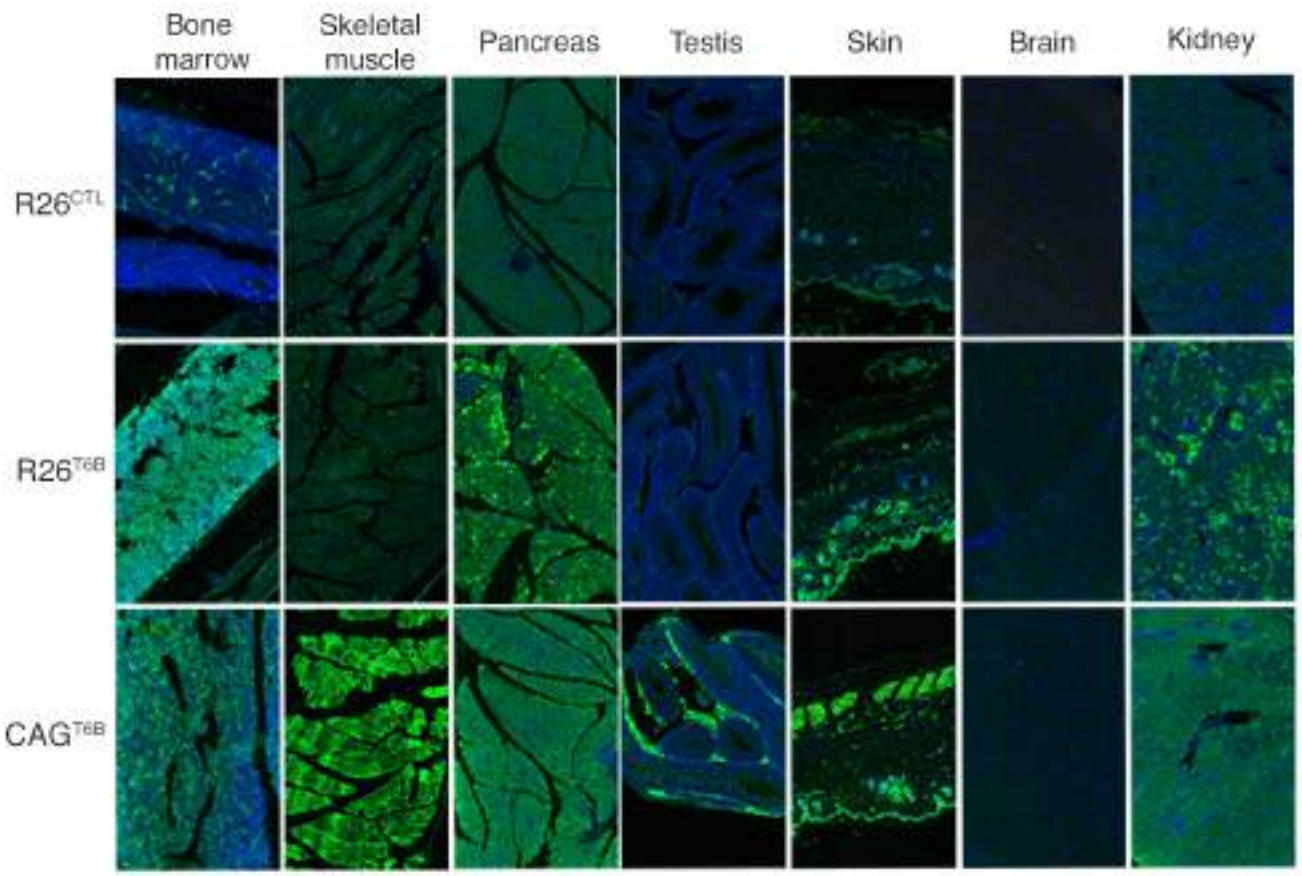

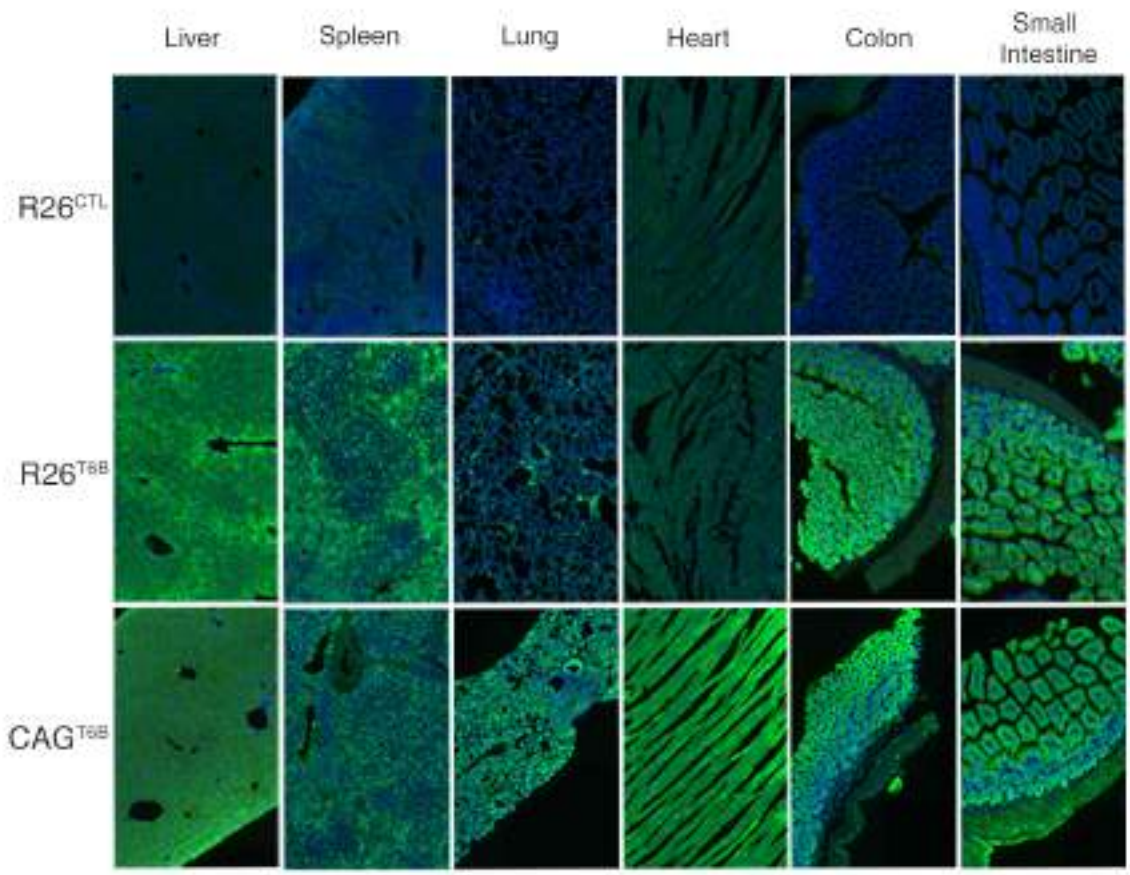

Figure 2-figure supplement 2

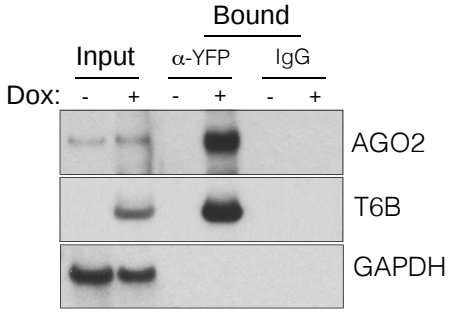

Figure 2-figure supplement 3

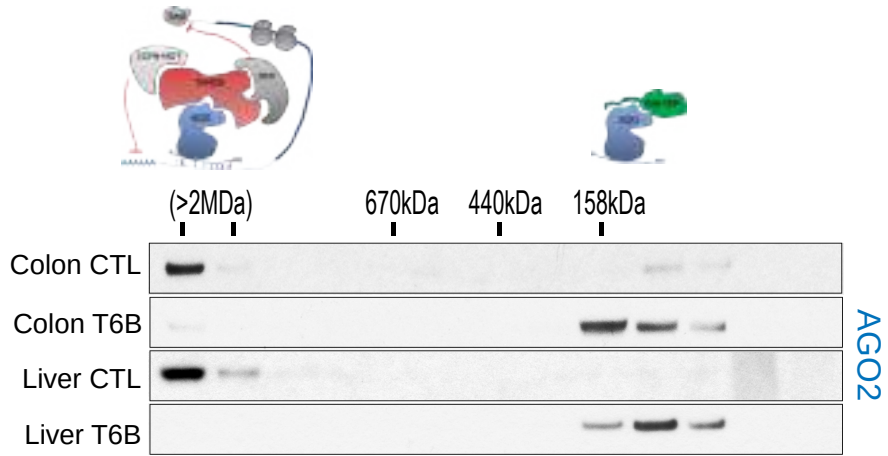

Figure 2-figure supplement 4

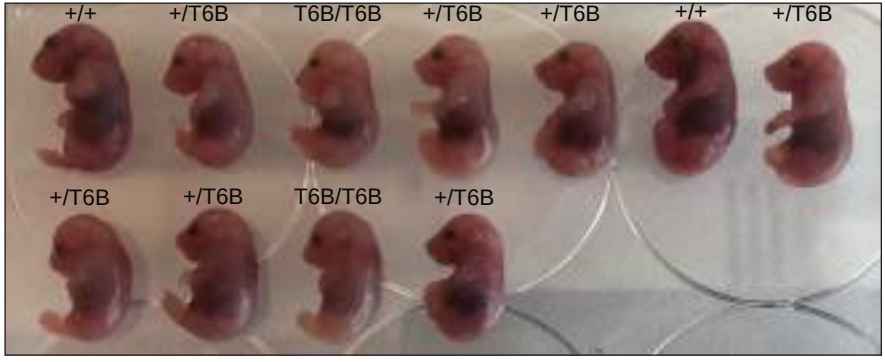

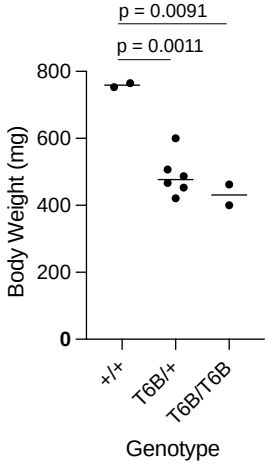

Figure 3-figure supplement 1

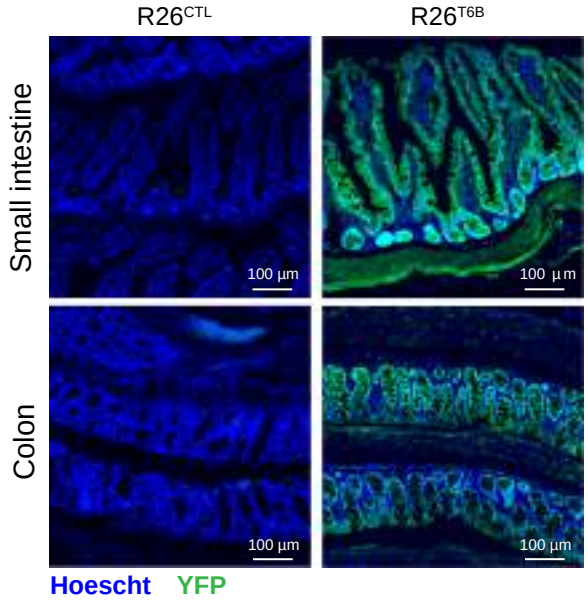

Figure 3-figure supplement 2

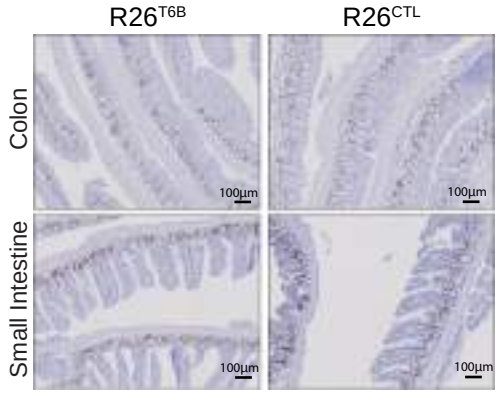

Figure 3-figure supplement 3

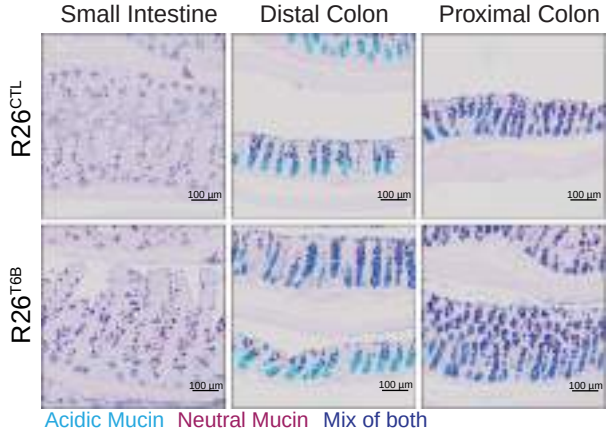

Figure 3-figure supplement 4

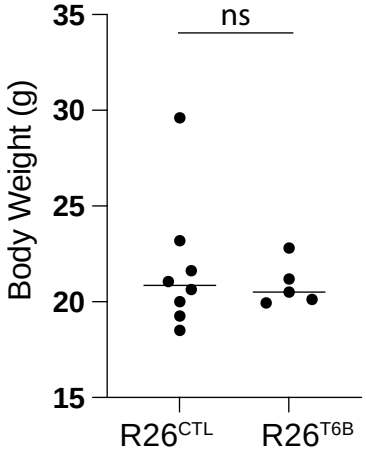

Figure 3-figure supplement 5

		CTRL (n=5)	T6B (n=5)	*P* value
RBC	$10^6/\mu L$	10.8 ± 0.483	10.7 ± 0.292	0.9225
HGB	g/dL	16.4 ± 0.589	14.8 ± 0.277	0.0052
HCT	%	57.0 ± 1.74	52.0 ± 0.631	0.0037
MCV	fL	52.8 ± 1.33	48.6 ± 0.858	0.0041
MCH	pg	15.2 ± 0.2	13.9 ± 0.195	0.0002
RDW	%	22.8 ± 0.342	25.5 ± 0.716	0.0019
RET	$10^3/\mu L$	564 ± 68.5	569 ± 76.5	0.9273
WBC	$10^3/\mu L$	7.46 ± 1.16	9.16 ± 1.23	0.2608
PLT	$10^3/\mu L$	990 ± 290	1270 ± 154	0.2728

Figure 3-figure supplement 6

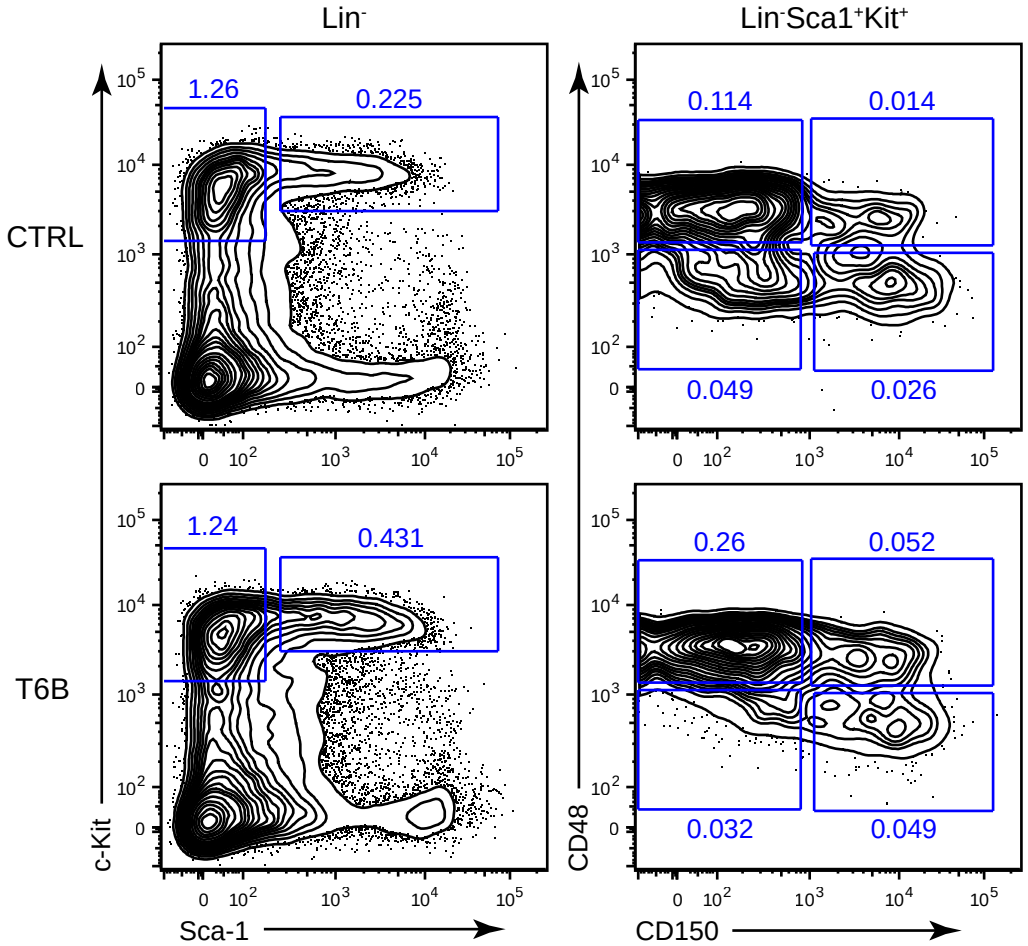

Figure 3-figure supplement 7

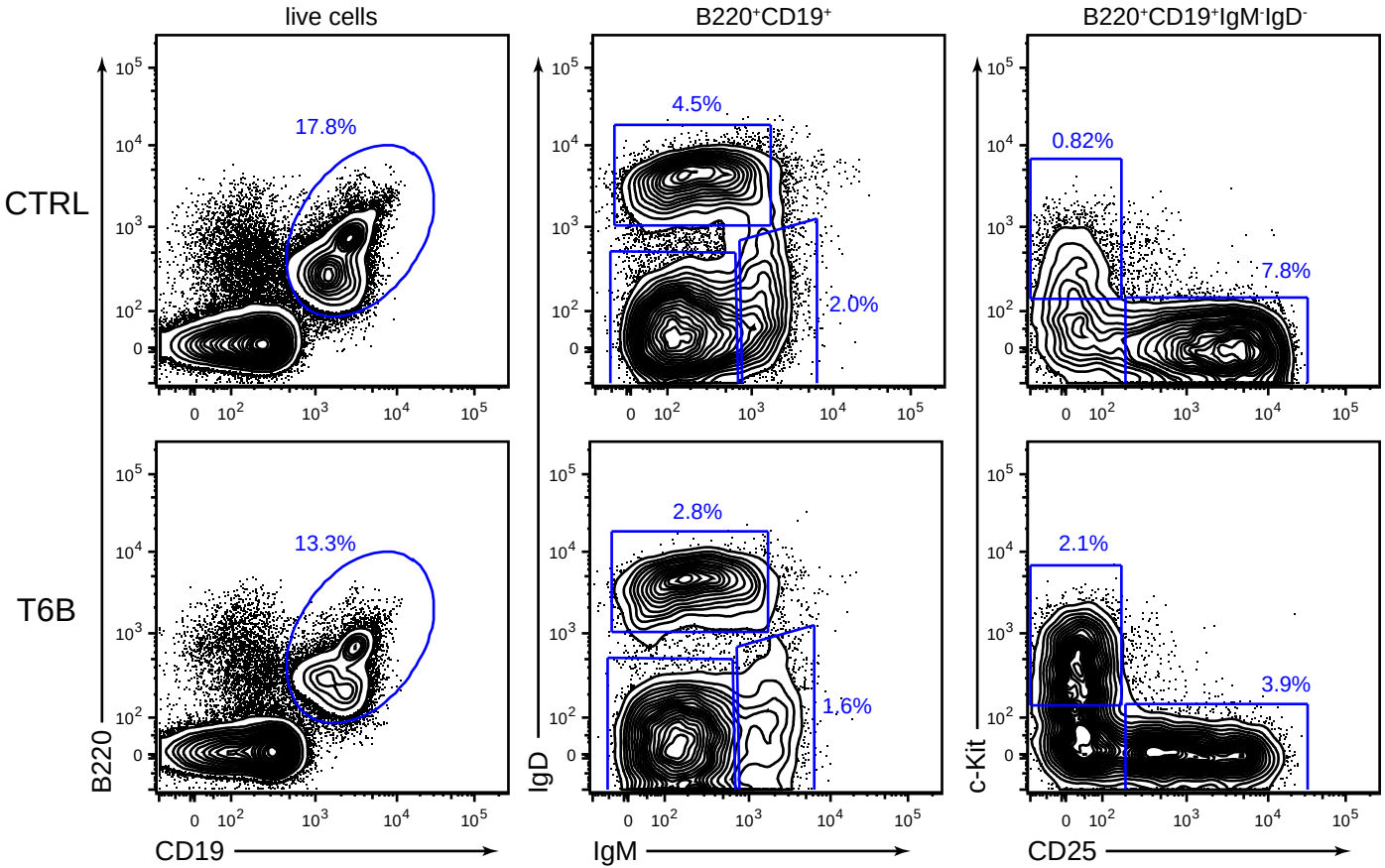

Figure 3-figure supplement 8

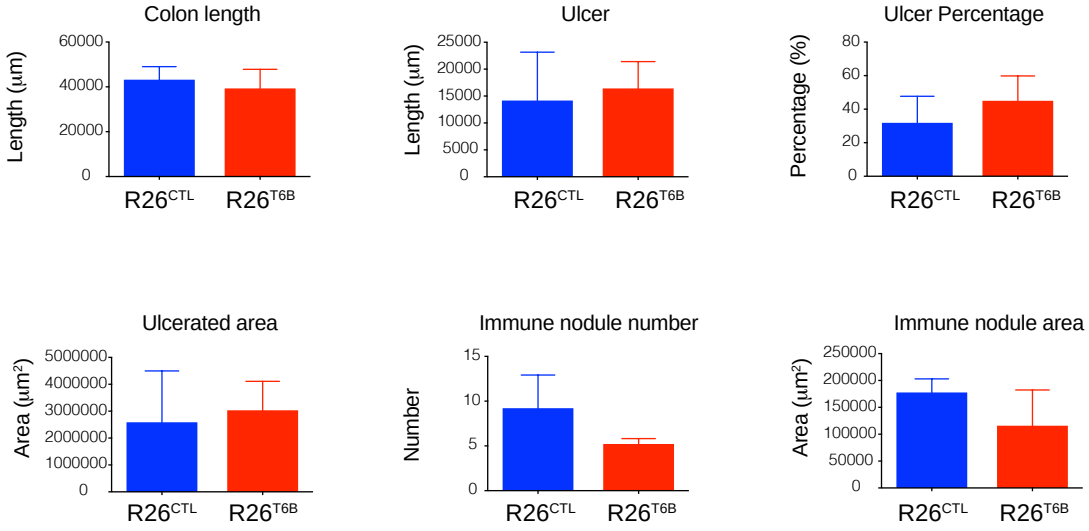

Figure 4-figure supplement 1

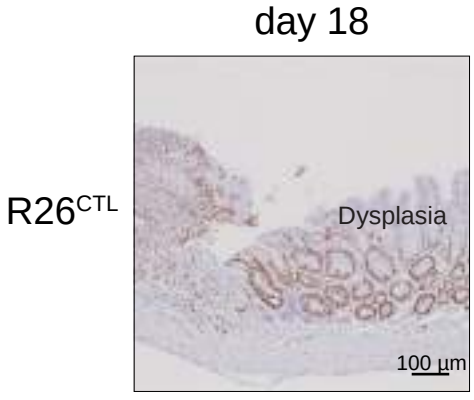

Figure 4-figure supplement 2

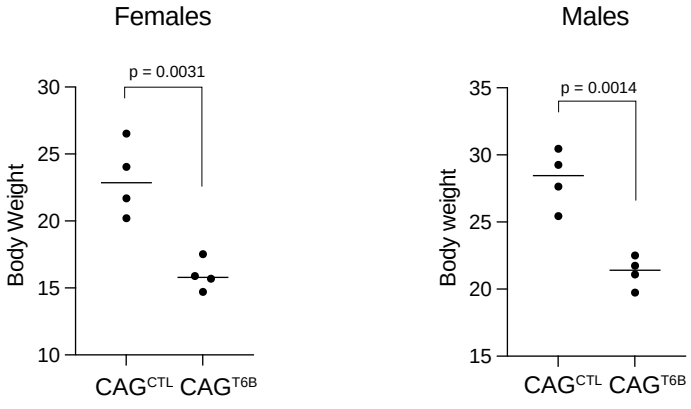

Figure 6-figure supplement 1

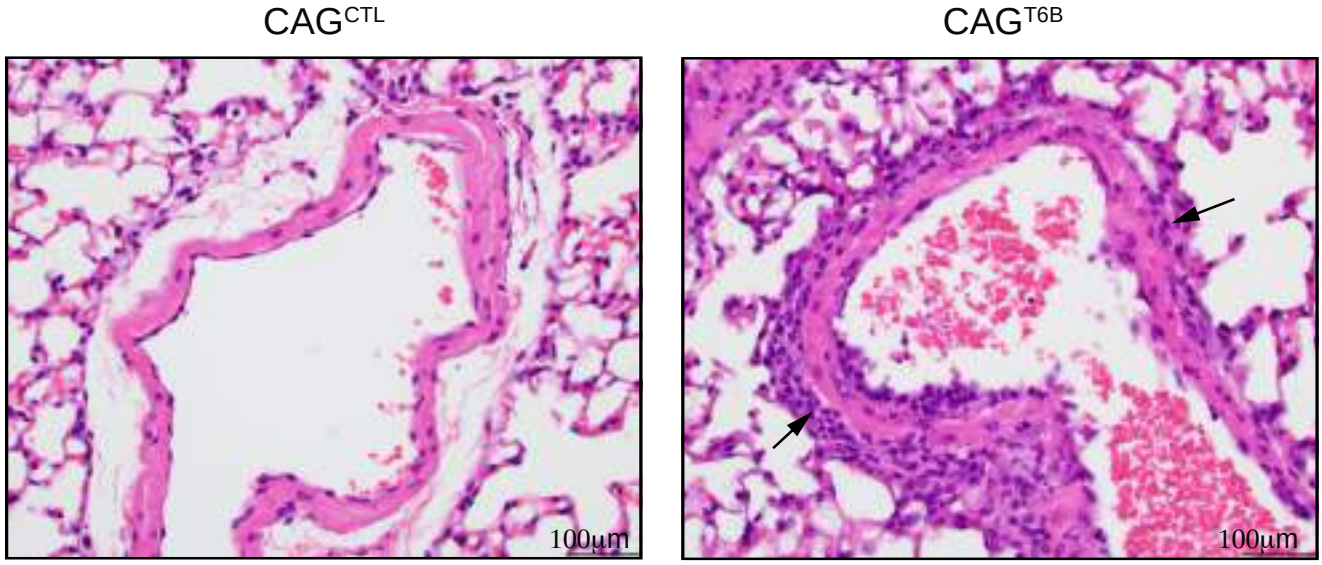

Figure 6-figure supplement 2

a

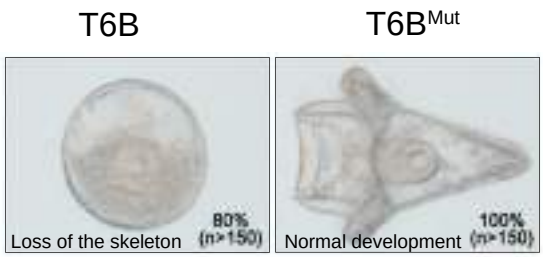

48h post-fertilization

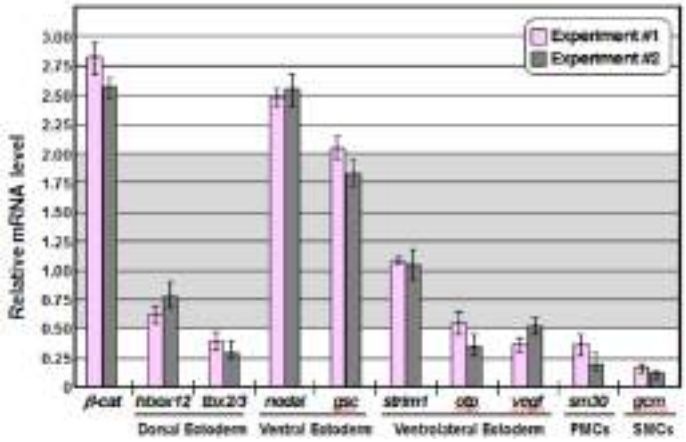

b

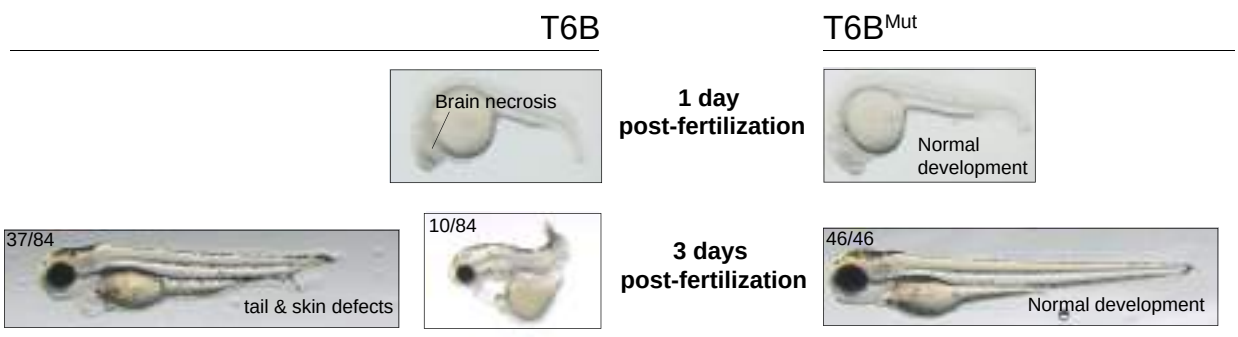

Figure 6-figure supplement 3